

---

## Effects of postglacial seawater intrusion on sediment geochemical characteristics in the Romanian sector of the Black Sea

Ruffine Livio <sup>1,\*</sup>, Deusner Christian <sup>2</sup>, Haeckel Matthias <sup>2</sup>, Kossel Elke <sup>2</sup>, Toucanne Samuel <sup>1</sup>, Chéron Sandrine <sup>1</sup>, Boissier Audrey <sup>1</sup>, Schmidt Mark <sup>2</sup>, Donval Jean-Pierre <sup>1</sup>, Scholz Florian <sup>2</sup>, Guyader Vivien <sup>1</sup>, Ker Stephan <sup>1</sup>, Riboulot Vincent <sup>1</sup>

<sup>1</sup> IFREMER, Département Ressources physiques et Ecosystèmes de fond de Mer (REM), Unité des Géosciences Marines, 29280, Plouzané, France

<sup>2</sup> GEOMAR Helmholtz Centre for Ocean Research Kiel, Wischhofstr. 1-3, D-24148, Kiel, Germany

\* Corresponding author : Livio Ruffine, email address : [livio.ruffine@ifremer.fr](mailto:livio.ruffine@ifremer.fr)

---

### Abstract :

Pore water and sediment geochemistry in the western Black Sea were investigated on long Calypso piston core samples. Using this type of coring device facilitates the recovery of the thick sediment record necessary to analyze transport-reaction processes in response to the postglacial sea-level rise and intrusion of Mediterranean salt water 9 ka ago, and thus, to better characterize key biogeochemical processes and process changes in response to the shift from lacustrine to marine bottom water composition. Complementary data indicate that organic matter degradation occurs in the upper 15 m of the sediment column. However, sulfate reduction coupled with Anaerobic Methane Oxidation (AOM) is the dominant electron-accepting process and characterized by a shallow Sulfate Methane Transition Zone (SMTZ). Net silica dissolution, total alkalinity (TA) maxima and carbonate peaks are found at shallow depths. Pore water profiles clearly show the uptake of K<sup>+</sup>, Mg<sup>2+</sup> and Na<sup>+</sup> by, and release of Ca<sup>2+</sup> and Sr<sup>2+</sup> from the heterogeneous lacustrine sediments, which is likely controlled by chemical reactions of silicate minerals and changes in clay mineral composition. Iron (Fe<sup>2+</sup>) and manganese (Mn<sup>2+</sup>) maxima largely coincide with Ca<sup>2+</sup> peaks and suggest a close link between Fe<sup>2+</sup>, Mn<sup>2+</sup> and Ca<sup>2+</sup> release. We hypothesize that the Fe<sup>2+</sup> maxima below the SMTZ result from deep Fe<sup>3+</sup> reduction linked to organic matter degradation, either driven by DOC escaping from the shallow sulfate reduction zone or slow degradation of recalcitrant POC. The chemical analysis of dissolved and solid iron species indicates that iron is essentially associated with clay minerals, which suggests that microbial iron reduction is influenced by clay mineral composition and bioavailability of clay mineral-bound Fe(III). Overall, our study suggests that postglacial seawater intrusion plays a major role in shaping redox zonation and geochemical profiles in the lacustrine sediments of the Late Quaternary.

---

## Highlights

► Geochemical analyses highlight multiple diagenesis processes occurring in the sediment. ► Intense methane seepages and organic matter degradation contribute to the sulfate reduction. ► Chemical of dissolved and mineral iron species indicate that iron is associated with clay minerals. ► In response to seawater intrusion, ion exchange, dissolution and reverse weathering reactions change the composition of clay constituting the sediment.

**Keywords** : Black sea, clay minerals, Danube delta, gas seeps, iron reduction, methane oxidation, sulfate reduction

44 The Black Sea has been investigated for decades, primarily because it is the largest  
45 anoxic basin on Earth and it represents a large hydrocarbon-producing province (Kosarev,  
46 2007; Robinson et al., 1996; Robinson, 1997). Previous investigations were diverse and  
47 integrated physical oceanography, petroleum geology, tectonics, paleoceanography,  
48 hydrology, and marine biology and ecosystem studies to reconstruct the history of the basin,  
49 capture its current dynamics and preserve its environmental quality and biodiversity. The  
50 Black Sea is connected to the Atlantic Ocean through the Marmara and the Mediterranean  
51 seas, and is characterized by two water masses: a salty water mass at the bottom supplied  
52 from the ocean, and a fresh water mass at the surface delivered by the rivers. The Black Sea  
53 hosts a large number of vigorous methane-rich seeps from the continental shelf to the deepest  
54 part of its basins that release gas high into the water column (Hillman et al., 2018a; Kessler et  
55 al., 2006a; Kessler et al., 2006b; Naudts et al., 2006; Roemer et al., 2012; Schmale et al.,  
56 2010a; Schmale et al., 2005; Schmale et al., 2011; Schmale et al., 2010b). These seeps play a  
57 pivotal role in the Black Sea methane cycling (Pape et al., 2008; Reeburgh et al., 1991;  
58 Schmale et al., 2010a) and are the major methane source responsible for the high  
59 concentrations measured in the water column (Greinert et al., 2006; Greinert et al., 2010;  
60 Reeburgh, 2007). However, a significant amount of methane generated in the sediment does  
61 not reach the water column (Wallmann et al., 2006) as it is partly stored as gas hydrates  
62 (Blinova et al., 2003; Bohrmann et al., 2003; Heeschen et al., 2011; Ker et al., 2019; Popescu  
63 et al., 2007; Zander et al., 2017) or oxidized within the anoxic sediment (Holmkvist et al.,  
64 2011; Jorgensen et al., 2004; Jorgensen et al., 2001; Meister et al., 2013; Niewohner et al.,  
65 1998; Reeburgh et al., 1991; Regnier et al., 2011; Reitz et al., 2011; Wallmann et al., 2006;  
66 Zander et al., 2020).

67 The chemical composition of pore water in the anoxic Black Sea surface sediments is  
68 significantly affected by the onset of the intrusion of seawater into the basin approximately 9

69 ka BP (Soulet et al., 2011b), giving rise to transient-state diffusion profiles and non-  
70 equilibrium chemical conditions. Thus, the natural setting is ideal to provide mechanistic  
71 insight and characterize dynamics of important diagenetic processes related to mineral  
72 dissolution, alteration or secondary mineral formation. Previous geochemical studies have  
73 shown that the sedimentary column of the Black Sea is highly reactive and particulate organic  
74 carbon (POC) degradation largely occurs in the upper part of the sediment (Egger et al., 2016;  
75 Henkel et al., 2012; Schouten et al., 2001). Methanogenesis, organoclastic sulfate reduction  
76 (SR) and anaerobic oxidation of methane (AOM) represent key reactions central to the Black  
77 Sea carbon cycling amongst the broad range of redox reactions that commonly lead to the  
78 vertical zonation of the sediment. Microbial iron and manganese reduction below the Sulfate  
79 Methane Transition Zone (SMTZ) contribute to organic matter degradation, and it is a topic  
80 of ongoing discussion if the reactions are driven by methane oxidation or the turnover of other  
81 organic or inorganic substrates (Egger et al., 2016). Previous studies have demonstrated the  
82 strong link between carbon, sulfur, iron and phosphate cycling and also suggest a strong  
83 coupling between methane turnover and silicate weathering (Aloisi et al., 2004a; Aloisi et al.,  
84 2004b; Egger et al., 2017; Egger et al., 2016; Henkel et al., 2012; Reitz et al., 2011;  
85 Wallmann et al., 2006). All of the aforementioned microbially influenced geochemical  
86 processes can significantly alter the chemistry of pore waters and sediment mineral  
87 composition.

88 Northern hemisphere climate variations during the last glacial and the Holocene  
89 strongly influenced the size of continental ice sheets and glaciers, and the global sea level.  
90 This affected the water level of the Black Sea/Lake as well as the sources and intensity of  
91 riverine input, resulting in varying accumulation of terrigenous sediments from different  
92 sources and with different rates (Huvaj and Huff, 2016; Özsoy and Ünlüata, 1997; Piper and  
93 Calvert, 2011; Stoffers and Muller, 1972; Wegwerth et al., 2016). In addition to input  
94 dynamics, local lithostratigraphy is influenced by internal dynamics resulting from sediment  
95 mobilization and re-deposition, slumping and slope failure events and the complicated  
96 functioning of the Danube deep sea fan (Constantinescu et al., 2015; Hillman et al., 2018b;  
97 Popescu et al., 2004; Xu et al., 2018), which connects the upper shelf with the deep basin.  
98 Historically, three sedimentary units were identified describing the general stratigraphy of  
99 Late Pleistocene and Holocene sediments in the Black Sea (e.g., Degens and Ross, 1972): a  
100 microlaminated coccolith ooze (Unit I, since ca. 2.76 ka BP; Lamy et al., 2006); an organic  
101 matter rich sapropel (Unit II, since ca. 8.5 ka BP; Soulet et al., 2011); and (Unit III) a banded  
102 lacustrine lutite. Recent efforts provided more detailed lithological and chronostratigraphical

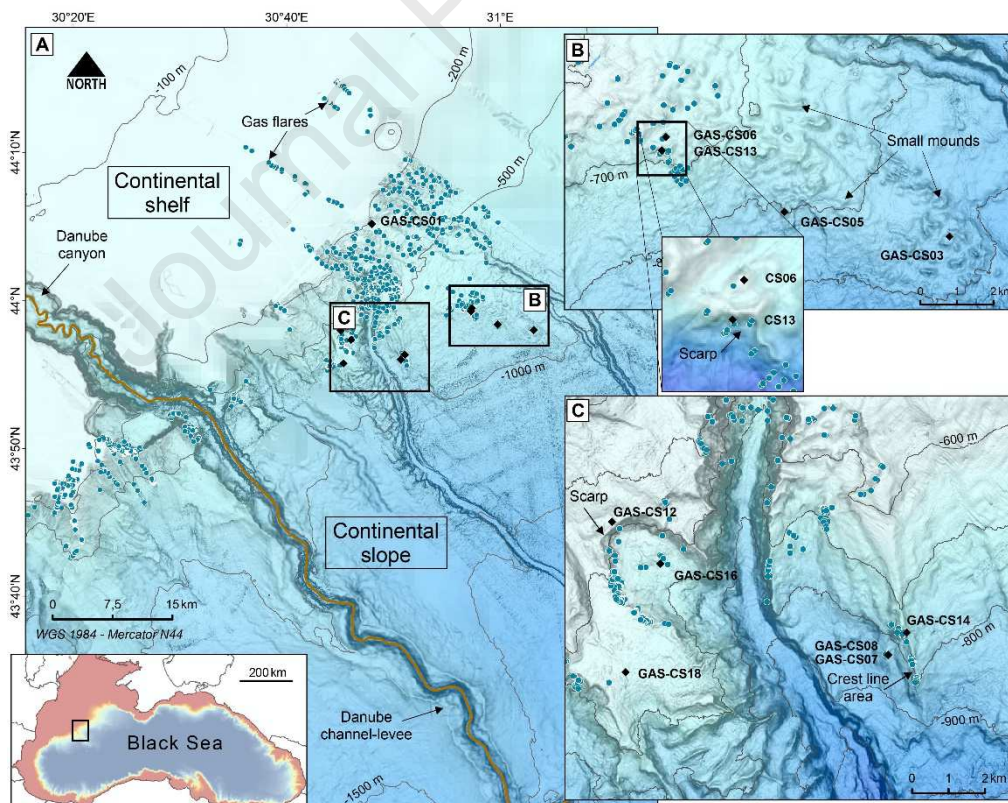
103 information from different parts of the Black Sea (e.g. Lamy et al., 2006; Kwiecien et al.,  
104 2008; Soulet et al., 2011; Nowaczyk et al., 2012; Soulet et al., 2018), still highlighting the  
105 complexity of building age model frameworks due to problems of constraining reservoir ages  
106 and sediment input on local and regional scales (Kwiecien et al., 2008; Soulet et al., 2011).  
107 The Danube River is considered to be the major source of sediment to the north-western  
108 margin of the Black Sea (Lericolais et al., 2013), especially during the ca. 32-17 ka period  
109 (Martinez-Lamas et al., 2020). Over this period, the river was characterized by high flood  
110 activity supplying huge amounts of sediment to the margin and the deep basin. Martinez-  
111 Lamas et al. (2020) demonstrated that the major sources of sediment have changed over that  
112 period, primarily because of the dynamics of the Alpine Ice sheets (AIS), but also that of the  
113 Fennoscandian Ice Sheet (FIS)(Soulet et al., 2013). Changes in the chemical composition and  
114 mineralogy of the deposited sediment are controlled by the relative inputs from the Danube  
115 tributaries connected to three main zones of the drainage basin (Martinez-Lamas et al., 2020).  
116 Thus, unlike the North-Eastern Alps, the Carpathians and the Dinarides are characterized by  
117 an abundance of kaolinite, and a low dolomite content. The Alpine glaciers provide illite-rich  
118 sediment, with a significant amount of smectite, chlorite, and dolomite; the two latter being  
119 mainly supplied from the inner Alpine.

120 In 2015, a study in the Romanian sector of the Black Sea has been undertaken on  
121 board the R/V Pourquoi pas? to map the distribution of fluid seeps and gas hydrates in the  
122 area, and to identify relationships between fluid migration and sediment destabilization,  
123 which could be observed from features apparently related to slumping and slope failure  
124 (Ballas et al., 2018; Riboulot et al., 2017; Riboulot et al., 2018). Special attention was also  
125 given to the understanding of the dynamics of the gas hydrate deposits (Ker et al., 2019), and  
126 the occurrence of multiple BSRs (Zander et al., 2017). The area was previously investigated,  
127 mainly to reconstruct its past climate and the functioning of the Danube delta (Constantinescu  
128 et al., 2015; Major et al., 2006; Popescu et al., 2006; Soulet et al., 2010). However, unlike  
129 other sectors of the Black Sea (Aloisi et al., 2004a; Aloisi et al., 2004b; Reitz et al., 2011;  
130 Wallmann et al., 2006), there are only few studies in this dynamic area (e.g. Jorgensen et al.  
131 2001, Knab et al. 2009, Egger et al. 2016) aimed to document geochemical processes in  
132 response to seawater intrusion and gas seepage. Hence, the purpose of this study is to  
133 contribute towards filling this gap by integrating geochemical analyses of pore water and  
134 sediment samples to decipher the coupling of element cycling in the upper tens of meters of  
135 the sedimentary column.

136

## 137 Description of the study area

138 Our study area is located in the Romanian water sector (Fig. 1) at the eastern part of  
 139 the main Danube canyon, where several other canyons have developed. In this area, evidence  
 140 for sediment instability and mass movement was found during cruise MSM-34 in 2013  
 141 (Bialas et al., 2014; Haeckel et al., 2015) and GHASS cruise in 2015 (doi:  
 142 [10.17600/15000500](https://doi.org/10.17600/15000500)). Acoustic surveys of the water column on both cruises showed that this  
 143 area is characterized by a large number of widespread gas expulsion sites at the seafloor,  
 144 bubbling up to several tens to hundreds of meters into the water column (Riboulot et al.,  
 145 2017). Sites of intense gas seepage indicate strong upward methane migration and discharge  
 146 in and from the anoxic Black Sea sediments. Accordingly, they have served for guiding  
 147 coring operation during the GHASS cruise. The cores were collected from water depths  
 148 between 240 m and 822 m. Core GAS-CS01 was collected at the shelf edge, and GAS-CS07,  
 149 08 and 14 along a crest, and the remaining ones on landslide scars or small seafloor  
 150 depressions. Riboulot et al. (2018) have shown that the pattern of the seep distribution is  
 151 related to the gas hydrate stability zone (GHSZ). Indeed the gas flares are primarily located on



152 the shelf and at the upper border of the GHSZ. Within the GHSZ seeps are positioned only at  
 153 the rim of landslide scars, and at specific location where faults reach the seafloor (Ker et al.,  
 154 2019).

155

156 Fig. 1: A) Bathymetric map of the Romanian sector of the Black Sea showing the Danube canyon and the  
 157 location of all cores recovered on the continental slope. The blue dots highlight the acoustic gas flares identified  
 158 in the water column during the GHASS cruise (Riboulot et al., 2017). B and C) Detailed views of the study area  
 159 with location of the cores. Core positioning was guided by the presence of gas flares, or other indications or  
 160 topographical features attributable to potential presence of shallow gas hydrates.

161

## 162 **Sampling and analyses**

### 163 *Coring and sampling*

164 During the GHASS cruise, the coring locations together with Penfeld measurements  
 165 were selected from previous acoustic and seismic surveys. A Calypso piston-corer was  
 166 deployed to collect long sediment cores with a length of up to ~35m. A total of 11 cores were  
 167 collected (Table 1) for geochemical, geophysical and geotechnical analysis. Once retrieved,  
 168 the Calypso cores were cut into 1m long round sections and transferred to the shipboard  
 169 laboratory for pore water sampling and processing at sea bottom temperature. The sediment  
 170 cores were sampled for pore water analyses immediately after the recovery.

171

172

Table 1: List of cores recovered and sampled for pore water analyses

Core name	Coordinates	Length/ cm	Water depth/ m
<b>GAS-CS01</b>	N44°05.188'; E30° 47.961'	3337	<b>240</b>
<b>GAS-CS03</b>	N43°58.030'; E31° 03.107'	2246	<b>842</b>
<b>GAS-CS05</b>	N43°58.3944'; E30° 59.7349'	1179	<b>794</b>
<b>GAS-CS06</b>	N43°59.4985'; E30°57.3139'	1970	<b>650</b>
<b>GAS-CS07</b>	N43°56.048'; E30°50.6635'	1234	<b>822</b>
<b>GAS-CS08</b>	N43°56.048'; E30°50.6635'	2080	<b>821</b>
<b>GAS-CS12</b>	N43°57.994'; E30°45.020'	2464	<b>547</b>
<b>GAS-CS13</b>	N43°59.298'; E30°57.234'	1381	<b>660</b>
<b>GAS-CS14</b>	N43°56.361'; E30°51.044'	542	<b>738</b>
<b>GAS-CS16</b>	N43°55.450'; E30°45.427'	2564	<b>685</b>
<b>GAS-CS18</b>	N43°55.777'; E30°45.301'	2740	<b>638</b>

173

174 Pore water was sampled using two different methods. Rhizon samplers were used as  
 175 long as the sediment was soft enough to insert the plastic tip of the sampler. A Rhizon  
 176 sampler (Rhizosphere Research Products, Netherlands) is a narrow elongated cylindrical filter  
 177 (0.2  $\mu\text{m}$  pore size; 5 cm long; 130  $\mu\text{L}$  volume) with a stiff plastic core (Seeberg-Elverfeldt et  
 178 al., 2005). Prior to use, the samplers were conditioned in distilled water ("MilliQ") for several

179 hours. Rhizon samplers are used to draw fluid from the sediment under vacuum, which is  
180 applied by attaching the samplers to 10 mL or 20 mL all-plastic syringes. The sampling took  
181 less than 12 hours. In addition to using Rhizon samplers, pore water was extracted using a  
182 pore water squeezer with N<sub>2</sub> gas of up to 5 bar as pressurizing agent and filtering the pore  
183 water through 0.2 µm Nuclepore cellulose acetate filters. The use of a second pore-water  
184 sampling method was necessary to recover sufficient water volumes for all analyses.  
185 Sediment samples for pore water pressing and sediment analysis were taken directly after  
186 recovery of the core from round sections or opened core halves. A 4-cm thick slice of  
187 sediment was removed from the working half at either the top or the bottom of the core  
188 section. Subsamples of the wet sediment were taken for measurement of sediment porosity, as  
189 well as for chemical and mineralogical analyses.

190

### 191 *Geochemical analysis*

192 Aliquots of the extracted pore water were sub-sampled for various onboard and shore-  
193 based analyses. Analyses for the nutrients NH<sub>4</sub><sup>+</sup>, PO<sub>4</sub><sup>3-</sup>, SiO<sub>4</sub><sup>4-</sup> as well as H<sub>2</sub>S were completed  
194 onboard using a Hitachi UV/VIS spectrophotometer. The respective chemical analyses  
195 followed standard procedures (Grasshoff et al., 1999), i.e. NH<sub>4</sub><sup>+</sup> was measured as indophenol  
196 blue, PO<sub>4</sub><sup>3-</sup> and SiO<sub>4</sub><sup>4-</sup> as molybdenum blue, and H<sub>2</sub>S as methylene blue. Total alkalinity (TA)  
197 was determined by titration with 0.02 N HCl using a mixture of methyl red and methylene  
198 blue as indicator. IAPSO seawater standard was used for calibration. Cl<sup>-</sup>, Br<sup>-</sup> and SO<sub>4</sub><sup>2-</sup>  
199 concentrations were determined by ion chromatography (METROHM 761 Compact). Cations  
200 were analyzed using ICP-OES (VARIAN 720-ES). Subsamples for ICP-OES analysis were  
201 acidified with 20 µl of conc. suprapure HNO<sub>3</sub> per 2 ml of porewater sample (i.e., pH < 1). All  
202 samples for shore-based analyses were stored refrigerated. Further analytical details,  
203 including analytical accuracies, precisions and detection limits, can be found in a previous  
204 study (Haffert et al., 2013).

205 Dissolved methane concentration was determined from a poisoned aliquot of wet  
206 sediment (10 µL of NaN<sub>3</sub>) by head-space coupled gas chromatography (Agilent GC-7890A  
207 coupled with a sampler HP7694). Stable carbon isotopic ratio of methane (δ<sup>13</sup>C/<sup>12</sup>C) was  
208 measured by using a continuous flow isotope ratio mass spectrometer (Thermo MAT253).  
209 Prior to oxidation of methane in a 1150 °C furnace, methane was separated from other gases  
210 in a coupled Thermo Trace GC (carrier gas: He; packed column: ShinCarbon, 1.5 m). Stable

211 isotope ratios are reported in the  $\delta$ -notation with respect to Vienna Pee Dee Belemnite  
212 (VPDB). Analytical precision of the reported isotopic composition is  $\pm 0.3$  ‰.

213 Wet sediment was collected for shore-based porosity, carbonate and element CNS  
214 analyses. Analyses were carried out using a EURO Element Analyzer (C/N/S configuration),  
215 prior and after removal of inorganic carbon with 1 M HCl. The analytical data are presented  
216 in percent of the total weight of dried sediment with an accuracy of 3%. Bulk chemical  
217 composition analysis of the sediment was carried out with a wavelength dispersive X-ray  
218 fluorescence spectrometer S8-Tiger from BRUKER. Mineral composition analysis of  
219 sediment samples was performed by X-ray diffractometry (XRD) using a D8 Advance model  
220 from BRUKER. Qualitative analysis of the diffraction pattern was carried out with the EVA  
221 software (BRUKER) for phase identification of unknown samples, while quantitative  
222 analyses were performed according to the Rietveld refinement method with the program  
223 TOPAS (BRUKER). Specific analyses were done to determine the clay mineral content  
224 according to a validated method commonly used for clay analysis (Holtzappel, 1985). The  
225 clay content was calculated by applying specific coefficients for the identified clays minerals  
226 (Underwood and Pickering, 1996). The results are given with an uncertainty of 10%. X-ray  
227 absorption near edge structure spectroscopy (XANES) (Calvin, 2013) was performed to  
228 investigate the mineralogy and the oxidation state of the mineral-bound iron. XANES spectra  
229 were recorded at beamline P64 of the synchrotron radiation source PETRA (Caliebe et al.,  
230 2019), which is operated by the Helmholtz research centre DESY in Hamburg, Germany. For  
231 the determination of the mineralogy, a set of reference spectra of iron-containing silicates  
232 (augite, biotite, montmorillonite, nontronite and olivine), oxides (ferrihydrite, goethite and  
233 hematite) and an iron sulfide (pyrite) were measured. The software package Athena (Ravel  
234 and Newville, 2005) was then used for linear fitting of the reference spectra to the XANES  
235 spectra of sediments from core GAS-CS01 (Scholz et al., 2016). The mean oxidation state of  
236 the sediments (fraction of ferric Fe,  $\text{Fe(III)}/\sum(\text{Fe})$ ) was obtained from the centroid position of  
237 the pre-edge structure (Scholz et al., 2016; Wilke et al., 2001).

238

## 239 **Results**

### 240 *Geochemical composition of pore water*

241 Pore water profiles of dissolved elements ( $\text{Cl}^-$ ,  $\text{SO}_4^{2-}$ ,  $\text{Ca}^{2+}$ ,  $\text{Mg}^{2+}$ ,  $\text{Na}^+$ ,  $\text{K}^+$ ,  $\text{Ba}^{2+}$ ,  $\text{Sr}^{2+}$ ,  
242  $\text{NH}_4^+$ ,  $\text{Br}^-$ ,  $\text{PO}_4^{3-}$ ,  $\text{SiO}_4^{4-}$ ,  $\text{HS}^-$ ,  $\text{Fe}^{2+}$  and  $\text{Mn}^{2+}$ ) and total alkalinity (TA) are presented in Fig.2.  
243 Chemical and isotope data of methane ( $\text{CH}_4$ ) are shown in Fig.3, and sediment geochemical

244 composition and mineralogy in Fig.4 and 5. Overall, pore water geochemical profiles show  
245 similar trends, and there is no significant effect of water depth or sample location on pore  
246 water profiles in Calypso cores retrieved on the slope, both close to and far from the shelf, for  
247  $\text{Cl}^-$ ,  $\text{SO}_4^{2-}$ ,  $\text{Ca}^{2+}$ ,  $\text{Mg}^{2+}$ ,  $\text{Na}^+$ ,  $\text{K}^+$ ,  $\text{Ba}^{2+}$ ,  $\text{Sr}^{2+}$ . However, pore water profiles from cores GAS-  
248 CS13 and GAS-CS14 appear as shifted and show significantly lower concentrations of  
249 dissolved elements compared to the other cores. The concentrations of  $\text{Cl}^-$ ,  $\text{Mg}^{2+}$ ,  $\text{Na}^+$ ,  $\text{K}^+$ , TA  
250 and  $\text{Br}^-$  decrease non-linearly with depth, resulting in profiles with a concave-down curvature,  
251 whereas concentrations of  $\text{Ca}^{2+}$ ,  $\text{Ba}^{2+}$ ,  $\text{NH}_4^+$ , and  $\text{Sr}^{2+}$  increase to a clear and pronounced  
252 maximum followed by a decrease with increasing depth. Among major cations  $\text{K}^+$ ,  $\text{Mg}^{2+}$  and  
253  $\text{Na}^+$ , the relative uptake of  $\text{Na}^+$  in the sediment is lowest, thus the shape of the  $\text{Na}^+$  profile is  
254 most similar to the  $\text{Cl}^-$  profile, whereas  $\text{K}^+$  is taken up within the upper 10 m of the sediment  
255 column. The  $\text{Mg}^{2+}$  profiles are characterized by different gradients with a near linear decrease  
256 in  $\text{Mg}^{2+}$  in the upper 11 - 13 m below seafloor (mbsf), whereas with greater sediment depth  
257 the gradient becomes less steep. Sulfate concentration decreases nearly linearly from values  
258 above 15 mM to values  $< 1$  mM. The SMTZ is reached for all cores at a depth shallower than  
259 6 mbsf. The SMTZ depth is even shallower than 1mbsf for cores GAS-CS07, 08, 13 and 14,  
260 which are the cores retrieved on crests. Elevated  $\text{CH}_4$  concentrations were measured over the  
261 entire length of the cores, and in few cases, increased  $\text{CH}_4$  concentrations were found even  
262 above the SMTZ. Regardless of the sample locations, methane is extremely depleted in  $^{13}\text{C}$ ,  
263 with  $\delta^{13}\text{C}-\text{CH}_4$  ranging between -62.71 and -72.11 ‰ (Fig.3). The profiles of  $\text{NH}_4^+$ ,  $\text{PO}_4^{3-}$ ,  
264  $\text{SiO}_4^{4-}$ ,  $\text{Fe}^{2+}$  and  $\text{Mn}^{2+}$  are very different from one core to another, and values show a large  
265 scattering. It has to be noted that the sampling and analytical procedures were not optimized  
266 for redox-sensitive species, thus the scatter could be related to procedural artefacts from  
267 handling of individual samples. However, this implies that elevated  $\text{Fe}^{2+}$  and  $\text{Mn}^{2+}$   
268 concentrations must be considered as lowest estimates, and *in situ* concentrations likely were  
269 higher. Nevertheless, clear  $\text{Fe}^{2+}$  and  $\text{Mn}^{2+}$  maxima were observed in most of the cores at  
270 depths between 8 and 15 mbsf.  $\text{NH}_4^+$  concentrations reached maximum values in the interval  
271 15 - 22 mbsf, with large differences in absolute  $\text{NH}_4^+$  concentrations in individual cores.

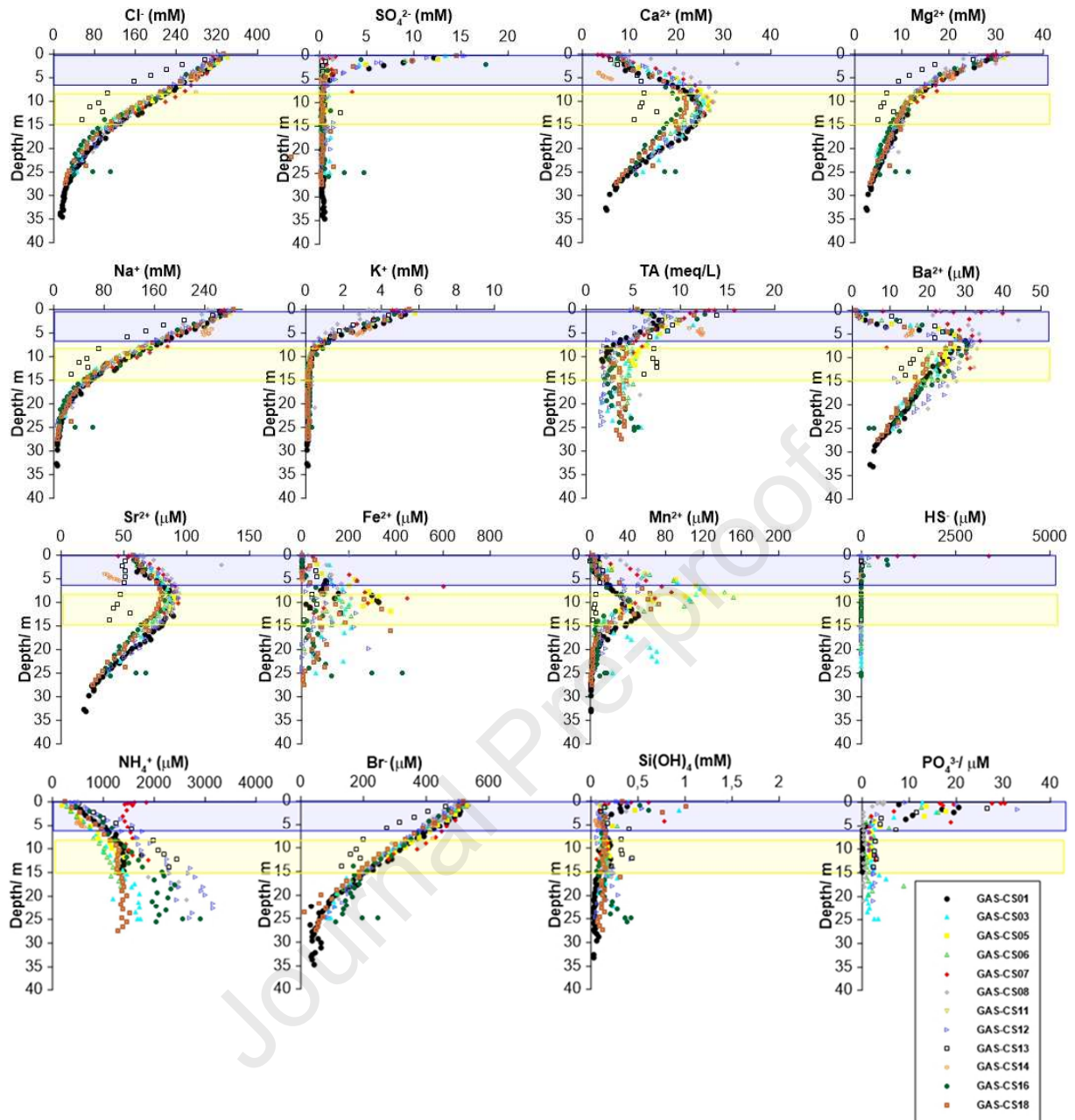
272

### 273 *Geochemical composition of sediment*

274 The organic carbon content decreases rapidly from more than 6 to less than 1 wt-%  
275 within the upper first meter of the sampled cores (Fig.4). The same rapid decrease is observed  
276 for the TIC content, which again increases within the horizon ~2.5 - 4 mbsf, and continues to  
277 increase throughout the sampled interval. The sediment shows high and stable contents of Al,

278 Si and Ti along the cores (Fig.5). Na and K contents are low but relatively constant  
279 throughout the sediment column. However, Fe and Mn contents, and also Mg and Ca  
280 contents, show larger relative differences within each individual core and in between cores.  
281 Sediment mineralogical analysis from cores GAS-CS01, CS03, CS07, CS12 and CS14 shows  
282 that clay minerals including mica account for 40 to 75 wt-%. This is followed by silicate  
283 minerals (feldspar, plagioclase, and quartz) and carbonate phases (mainly calcite and  
284 dolomite). The calcite content remains relatively constant except for few samples collected at  
285 the upper part of cores GAS-CS01 and GAS-CS12. The dolomite content is slightly lower  
286 than that of calcite and decreases towards the water-sediment interface. Amongst clay  
287 minerals, illite is the dominant species and accounts for more than 60% of the total clay  
288 mineral fraction (Fig.4). Smectite accounts for 5-20 % of the total clay mineral fraction, and  
289 kaolinite and chlorite both usually contribute to less than 10 %. For individual cores, we  
290 observe variable trends in clay mineralogy. In GAS-CS01, highest illite (> 90 %) and lowest  
291 smectite contents (<10 %) are observed in the narrow interval 4 – 6 mbsf. Below this interval,  
292 down to a depth of 22 – 24 mbsf, lower illite (70 %) and higher smectite (20 %) and kaolinite  
293 contents (8 %) are found. Below 24 mbsf, this trend is again reversed with higher illite (80  
294 %), and lower smectite (10 %) and kaolinite contents (2 %). In CS01, the chlorite content  
295 increases continuously with depth. However, these relations between clay mineralogy and  
296 depth cannot easily be transferred to other cores, which clearly indicates differences in  
297 lithology and sediment deposition histories between core locations. Mineral data variability is  
298 partly reflected in solid phase element profiles. In GAS-CS01, the element composition  
299 profile (Fig.5) shows a change in Mg content, which smoothly shift from lower to higher  
300 values at a depth of 22 – 24 mbsf. This trend appears to be associated with shifts in Si, Al, K,  
301 and Fe contents. Ca contents show considerable variability when comparing different cores,  
302 which is not reflected in pore water profiles.

303



304

305

306 Fig. 2: Pore water depth profiles of dissolved ion concentrations. Grey layer indicates the SMTZ, and yellow  
 307 layer corresponds to the interval of increased iron concentrations.

308

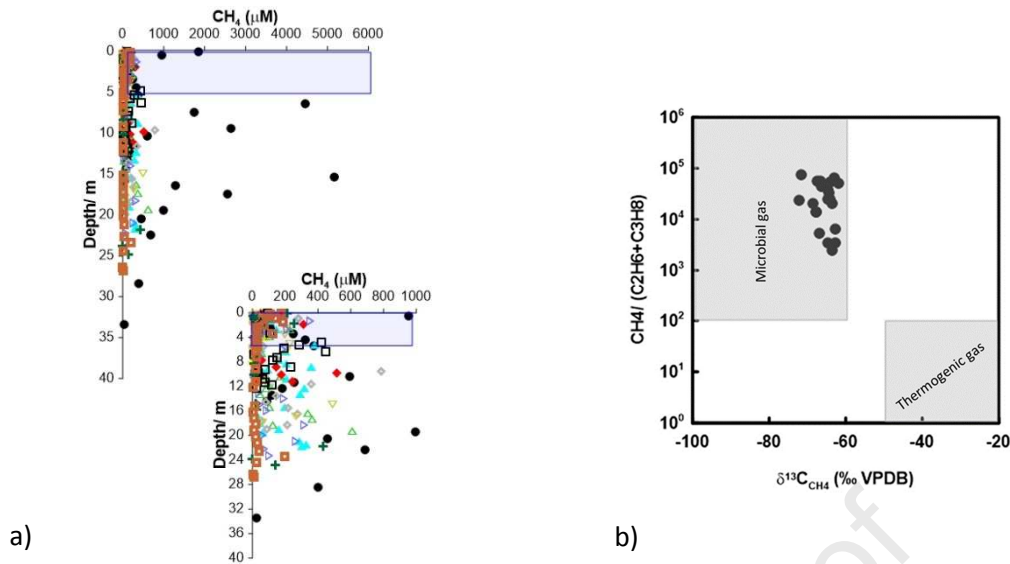
309

310

311

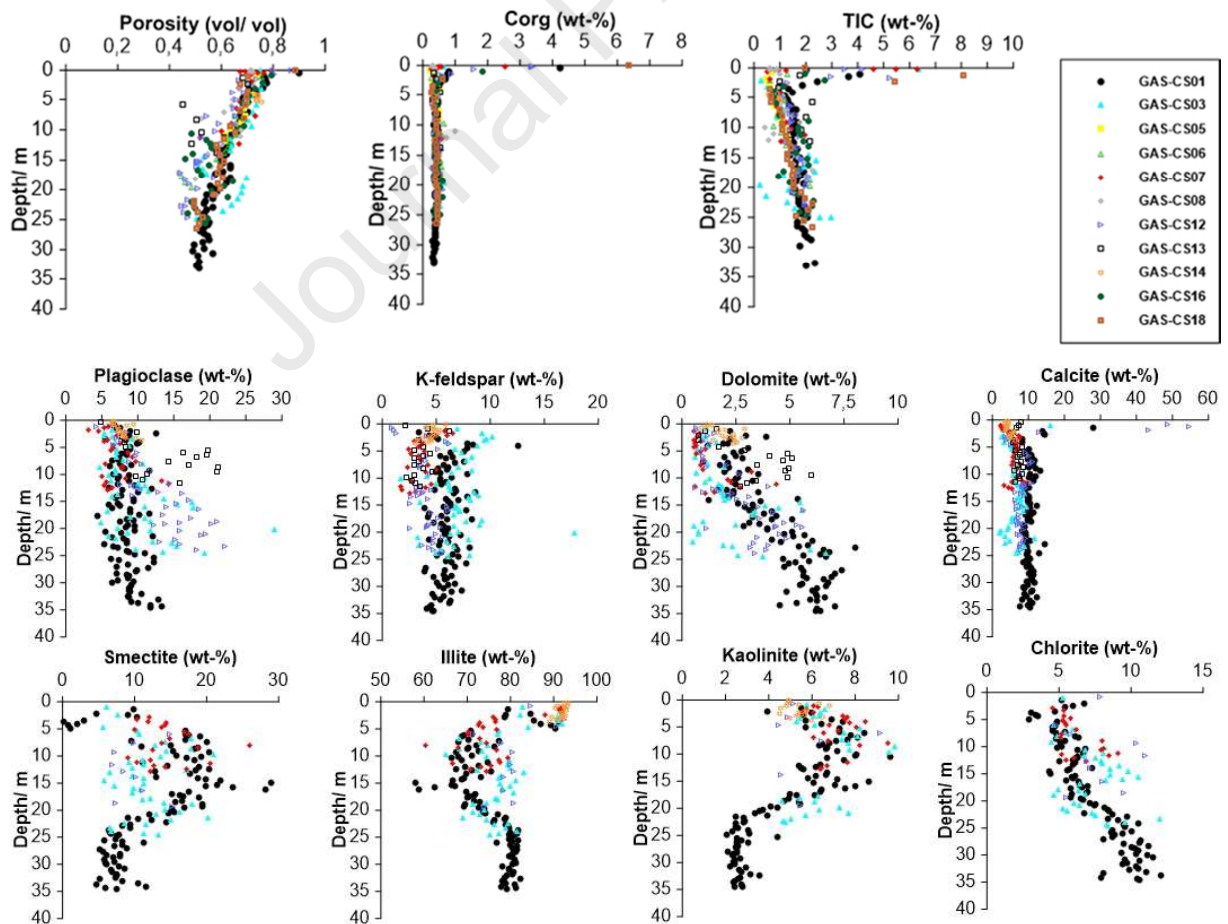
312

313



315 Fig. 3: a) Pore water depth profiles for dissolved methane concentration, and b) Diagram of  $\delta^{13}\text{C}$  of methane vs.  
 316 ethane and propane molecular compositions for the studied venting gases diagram modified after Bernard et al.  
 317 (Bernard et al., 1978). For the color code of Fig.3a, the reader should refer to Fig.2.

318  
 319



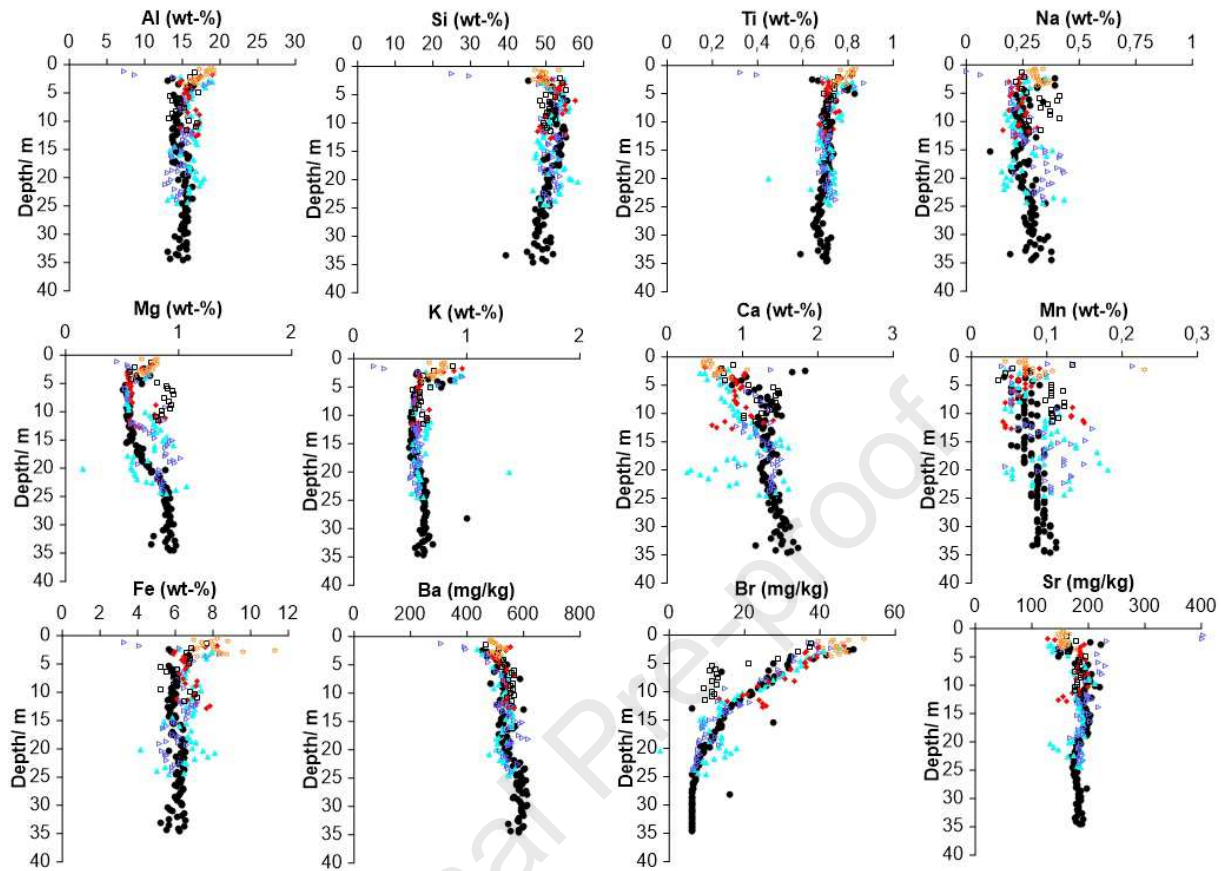
320

321

322 Fig. 4: Solid phase depth profiles of porosity, carbon fractions and mineralogy. Note that the clay fractions were  
 323 calculated from the total amount of clay only after separation from the other minerals present in the sediment.

324

325



326

327 Fig. 5: Solid phase depth profiles of chemical composition (For the color code, the reader should refer to Fig.2)

328

329

330 **Discussion**331 *Lithology and stratigraphic alignment*

332

333

334

335

336

337

338

339

340

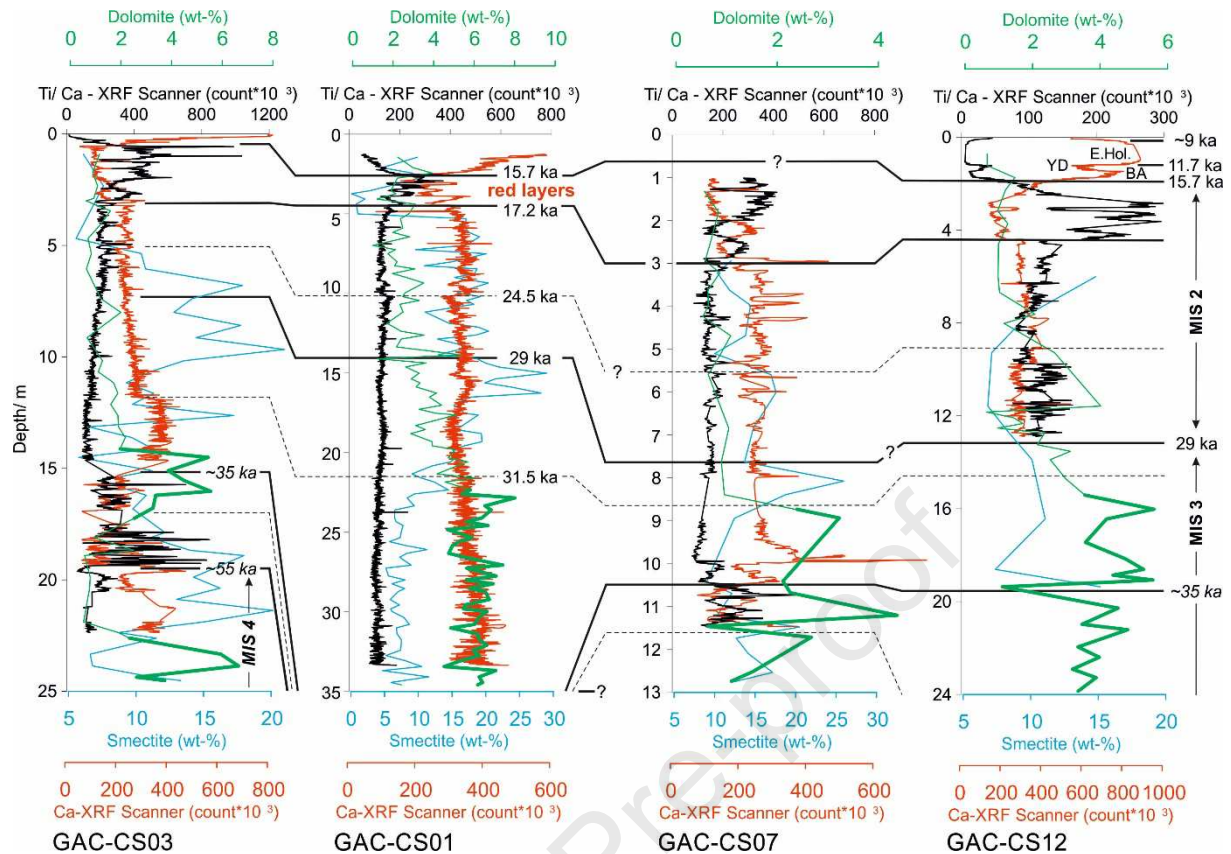
341

342

In accordance to known lithological variability, Calypso cores from this study showed substantially different solid phase element and mineral profiles (Figs. 4 & 5). To better distinguish geochemical effects in response to seawater intrusion from lithological changes, we compared specific time windows with known climatic and environmental conditions for four cores from different locations across the northwest Black Sea margin (Fig. 6), GAS-CS01, GAS-CS03, GAS-CS07 and GAS-CS12. A detailed analysis of core GAS-CS01 collected at the shallowest site was recently presented in Martinez-Lamas et al. (2020), with a detailed age model based on the evaluation of chemical, mineralogical and sedimentological markers in comparison with the well-studied core MD04-2790 (Soulet et al., 2011a). The study showed that core GAS-CS01 contains sediments of up to 33 ka BP, belonging to Unit III. The lacustrine-marine (L-M) transition Unit II and the marine Unit I were not clearly

343 identified. However, although it is not well resolved, Unit II was recovered in core GAS-  
344 CS12 suggesting the L-M transition at very shallow depth in the first tens of centimeters of  
345 cored sediment (Fig. 6). Sedimentary Ca-XRF counts and Ca/Ti ratios, together with the clay  
346 mineralogy, allowed the stratigraphic correlation of three additional cores (GAS-CS03, CS07  
347 & CS12) against the well-dated sediment core GAS-CS01 (Fig. 6). The correlations were  
348 realized, for example, through the recognition of (i) the Red Layers deposited ca. 17.2-15.7 ka  
349 (very low XRF-Ca values; (Soulet et al., 2013; Soulet et al., 2011a)); (ii) Peaks in dolomite  
350 content (green bold lines) indicating the influence of the Eastern Alps on the local  
351 sedimentation at the MIS 3/2 transition (Martinez-Lamas et al., 2020) and possibly during  
352 MIS 4, with potential contribution from low-temperature proto-dolomitization (Liu et al.,  
353 2019); (iii) the regional imprint of the Dansgaard/ Oeschger (D/O) variability of MIS 3  
354 recognized in the SE Black Sea during ca. 35-60 ka through large variations in the carbonate  
355 content (Wegwerth et al., 2015) (Fig. 6). One can clearly see that the cores GAS-CS03 and  
356 GAS-CS07 are characterized by a much lower sedimentation rate compared to GAS-CS01  
357 and GAS-CS12. Furthermore, in agreement with previous studies (Soulet et al., 2013; Soulet  
358 et al., 2011a), Martinez-Lamas et al. (2020) showed that sediment deposition on the NW  
359 Black Sea margin was highly variable at the end of the last glacial period due to the waxing  
360 and waning of the AIS and FIS in response to northern hemisphere climate variability. For the  
361 time interval prior to the deposition of the red layers during ca. 17.2-15.7 ka BP, hyperpycnal  
362 floods from the Danube River were identified as the main sediment source, and sediment  
363 deposition and burial of reactive minerals under lacustrine oxic bottom water conditions was  
364 much more rapid than modern sedimentation. The analysis of clay mineralogy and Nd isotope  
365 signatures of the Danube and its main tributaries suggested that early periods of meltwater  
366 release during 32.5-30.5 ka BP supplied smectite-poor, chlorite and dolomite-rich sediments  
367 from Eastern Alpine domains (Martinez-Lamas et al., 2020). Thereafter between 30 and 29 ka  
368 BP, higher smectite and kaolinite contents suggest that the signals of the sediment  
369 contribution from the Danube drainage basin with Dinarides and Carpathians were not  
370 overprinted by the Alpine contribution (Martinez-Lamas et al., 2020). Meltwater pulses from  
371 the Dniepr basin during the red layer interval supplied illite-rich sediments (Soulet et al.,  
372 2013).

373



374  
375

376 Fig. 6: Age-depth model derived from tentative stratigraphic correlations between cores GAS-CS01 (Martinez-  
377 Lamas et al. 2020), GAS-CS03, GAS-CS07 and GAS-CS12 (this study). The upper part of core GAS-CS07 was  
378 heavily charged in gas and not reliable for XRF analysis. Ages older than ~33.5 ka (*i.e.* base of GAS-CS01; in  
379 italic) are given according to the recognition of stratigraphical features observed in the SE Black Sea (Wegwerth  
380 et al., 2015). Peaks in dolomite content (green bold lines) indicate the influence of the Eastern Alps on the local  
381 sedimentation (see Martinez-Lamas et al., 2020 for details). All the sedimentary sequences studied here  
382 correspond to the lacustrine Unit III of Ross & Degens (1974). BA: Bölling-Alleröd; E.Hol.: Early Holocene;  
383 MIS: Marine Isotope Stage; YD: Younger Dryas.

384

### 385 *Transport-reaction characteristics of major ions*

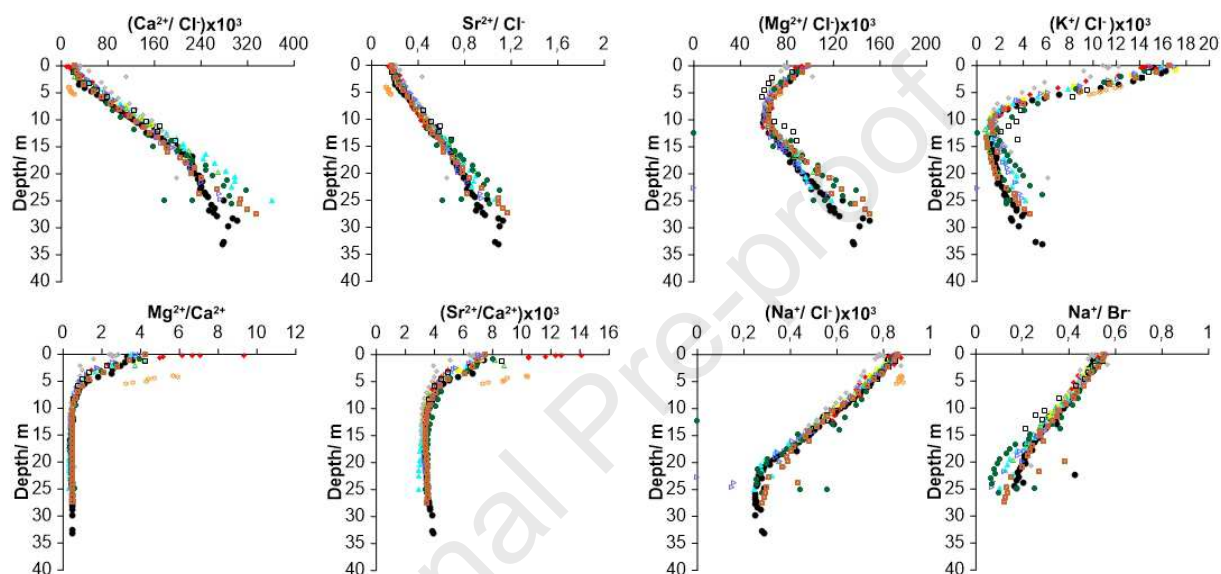
386 The shape of the pore water profiles illustrates the transport of dissolved species from  
387 today's Black Sea marine bottom waters into the lacustrine sediment since the reconnection  
388 with the Mediterranean Sea about 9 ka ago (Soulet et al., 2011b). The Cl<sup>-</sup> profiles have a  
389 slightly concave down shape and show a continuous decrease in salt concentration indicating  
390 the transient state of seawater infiltration. Diffusion is the dominant transport process of pore  
391 water species at most locations, and clear evidence for disturbances of profiles by recent  
392 sediment mass movement through slumping and slope failure events (Hillman et al., 2018b;  
393 Riboulot et al., 2017) is not found for most cores. Gas hydrates were recovered throughout  
394 core GAS-CS14, therefore the concentrations of dissolved elements might be affected by gas

395 hydrate dissociation after core recovery. However, a dilution effect is clearly visible only for  
396 Ca and Sr in the upper 5 m of sediment, and not for the other dissolved elements. Therefore,  
397 hydrate dissolution is not responsible for the low Ca and Sr concentrations. Other processes  
398 that we are unable to identify from our dataset might have affected pore water profiles at this  
399 location. Core GAS-CS13 also shows characteristically different pore water profiles,  
400 especially when comparing with core GAS-CS06, the closest core that is located less than 1  
401 km away. Unlike in core GAS-CS14, there was no evidence for gas hydrates in core GAS-  
402 CS13, which was located on an erosional feature (Fig.1). Thus, one possible explanation for  
403 the difference of the pore water profiles is that the erosion process has led to loss of surficial  
404 sediment, shifting dissolved element concentration to lower values. In principal, upward fluid  
405 migration and gas emission could have affected the pore water profiles; however, none of  
406 these impacts is obvious from our geochemical data. Another explanation for the difference in  
407 pore water profiles from cores GAS-CS13 and GAS-CS06 could be disturbances from the  
408 coring operation resulting in the loss of the surficial part. Indeed, the measured chloride  
409 concentrations at the uppermost part of all collected cores are lower than the Black Sea  
410 bottom water (Bohrmann et al., 2003; Soulet et al., 2010; Zander et al., 2020), and vary  
411 between 319 and 339 mM. Core depths have been corrected based on the response of the  
412 sensors monitoring the displacement of the piston, which provides a measure of reliability and  
413 quality of the coring. However, the loss of the upper sediment cannot be discarded, and  
414 comparison with the long piston core studied by Soulet et al. (2010) showed the lowest  
415 chloride concentrations of 311, 319 and 297 mM in cores GAS-CS01, GAS-CS08 and GAS-  
416 CS13 at ~1.5 mbsf, 2 mbsf, and 3 mbsf, respectively. For our present study, such an  
417 additional depth correction due to sediment loss has not been applied, as it does not change  
418 the sediment zonation proposed below. Profiles from core GAS-CS16 include two outlying  
419 data points at the bottom that likely result from seawater contamination.

420 The pore water profiles exhibit three intervals where significant changes of element  
421 gradients are observed; at 8 - 15 mbsf with distinct maxima of  $\text{Ca}^{2+}$ ,  $\text{Fe}^{2+}$  and  $\text{Mn}^{2+}$   
422 concentrations, at 22 - 24 mbsf, which coincides with a change of the marine water  $\text{Na}^+$   
423 gradient, and at 31 - 33 mbsf as the current depth of marine  $\text{Cl}^-$  penetration (Fig.2). In this  
424 transient-state transport-reaction scenario,  $\text{Cl}^-$  is considered as the most conservative  
425 dissolved species. Thus, the change of dissolved element: $\text{Cl}^-$  ratios indicates the diagenetic  
426 release or retention of reactive species (Fig.7). Decreasing  $\text{K}^+:\text{Cl}^-$  and  $\text{Mg}^{2+}:\text{Cl}^-$  ratios in the  
427 upper sediment column (shallower than 11 - 13 mbsf) indicate the uptake of  $\text{K}^+$  and  $\text{Mg}^{2+}$  by  
428 the sediment.  $\text{Ca}^{2+}:\text{Cl}^-$  and  $\text{Sr}^{2+}:\text{Cl}^-$  ratios steadily increase with depth, showing the relative

429 enrichment of  $\text{Ca}^{2+}$  and  $\text{Sr}^{2+}$  in the pore water. Below the  $\text{Ca}^{2+}$  maxima (11 -13 mbsf),  
 430  $\text{Sr}^{2+}:\text{Ca}^{2+}$  and  $\text{Mg}^{2+}:\text{Ca}^{2+}$  ratios remain constant, suggesting a tightly coupled release of  $\text{Ca}^{2+}$ ,  
 431  $\text{Mg}^{2+}$  and  $\text{Sr}^{2+}$ . These observations provide evidence for pronounced ion exchange capacities  
 432 of lacustrine clay minerals, which mainly results in the uptake of  $\text{K}^+$  and  $\text{Mg}^{2+}$ , and the release  
 433 of  $\text{Ca}^{2+}$  and  $\text{Sr}^{2+}$ . Further, the simultaneous release of  $\text{Ca}^{2+}$  and  $\text{Mg}^{2+}$  in the deeper sediment  
 434 column (below 11 - 13 mbsf) indicates dissolution or alteration of silicate and/or carbonate  
 435 minerals, which could not be constrained in this study.

436



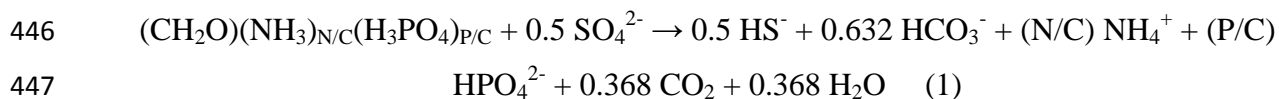
437  
 438 Fig. 7: Ratio of selected pore water species relative to chloride, calcium and bromide (For the color code, the  
 439 reader should refer to Fig.2)

440

#### 441 *Organic matter degradation and terminal electron-accepting processes*

442  $\text{NH}_4^+$  profiles suggest that organic matter degradation and carbon remineralization are  
 443 more pronounced in the upper 15 mbsf of the cored sediments than below. The organic matter  
 444 degradation is coupled to organoclastic sulfate reduction (Eq.1).

445



448

449 However, anaerobic oxidation of methane (AOM) largely contributes to sulfate turnover in  
 450 Black Sea sediments (Eq.2), and defines the depth of the SMTZ (Borowski et al., 1999).

451



453

454 The correspondence of the depths of  $\text{SO}_4^{2-}$  depletion and TA maxima suggests a dominant  
455 role of sulfate-dependent AOM, which is driven by upward diffusion of microbial methane  
456 produced by intense methanogenesis. This observation is corroborated by former studies  
457 estimating that AOM accounts for nearly 70% of total  $\text{SO}_4^{2-}$  turnover in typical Black Sea  
458 sediments (Egger et al., 2016; Jorgensen et al., 2001). Closer to methane seeps, AOM  
459 becomes even more dominant. The sulfate-depleted sediment below the SMTZ is  
460 undersaturated with respect to barite. Therefore, barite undergoes dissolution releasing  $\text{Ba}^{2+}$   
461 into the pore water in the interval 5-9 mbsf, beneath the AOM interval (Haeckel, 2006;  
462 Henkel et al., 2012; Noethen and Kasten, 2011). Very shallow SMTZ depths were determined  
463 for cores GAS-CS07, CS08, CS13 and CS14, suggesting enhanced upward methane migration  
464 at these sites (Jorgensen et al., 2004; Jorgensen et al., 2001; Zander et al., 2020). This is  
465 supported by evidence of both gas hydrates and gas emission at the crests, where these four  
466 cores were retrieved. The elevated methane concentrations observed above the SMTZ also  
467 indicate enhanced upward  $\text{CH}_4$  transport or limited AOM efficiency (Knab et al., 2009).  
468 Sulfide ( $\text{HS}^-$ ) becomes fully depleted below 1 mbsf in all cores although values as high as 3.4  
469 mM were measured at the first meter of sediment (Fig.2), which indicates efficient sulfide  
470 removal through iron sulfide precipitation. Usually sedimentary iron acts as the dominant  
471 sulfide sink, leading to the accumulation of pyrite and other iron-sulfur minerals (Canfield et  
472 al., 1992; Gregory et al., 2019; Jorgensen et al., 2004; Lyons, 1997; Meister et al., 2019;  
473 Neretin et al., 2001).

474 Thus, the transient increase of dissolved  $\text{Fe}^{2+}$  and  $\text{Mn}^{2+}$  concentrations below the SMTZ  
475 observed in this study (Fig.7) is not clearly related to  $\text{HS}^-$  profiles as found from previous  
476 studies (Jorgensen et al., 2004; Jorgensen et al., 2001; Zander et al., 2020), which indicates  
477 high iron and manganese reduction activities and confirms bioavailability of Fe(III) below the  
478 SMTZ, similar to recent findings (Egger et al., 2016; Jorgensen et al., 2004; Kraal et al.,  
479 2019). The presence of Fe(III) is in accordance with sedimentation characteristics and oxic  
480 bottom water conditions during the last glacial, and rapid burial of Fe(III)-bearing minerals  
481 may explain the positioning of the deep iron reduction zone. However, it is neither obvious  
482 which electron donor is used for deep iron reduction, nor if the positioning of the iron  
483 reduction zone is linked to the lacustrine-marine transition or to the presence of a distinct iron  
484 pool. Microbial iron reduction was likely an important process prior to seawater inflow under  
485 methanogenic conditions, since methanogenesis and iron reduction are largely compatible,  
486 and there is evidence that methanogenic organisms can shift metabolic capabilities towards

487 iron reduction in case of iron availability (Bar-Or et al., 2017; Oni et al., 2015; van Bodegom  
488 et al., 2004; Vigderovich et al., 2019; Zhang et al., 2012). Thus, the deep iron reduction  
489 activity below the SMTZ strongly suggests iron mobilization from a former refractory iron  
490 pool, or a distinct shift in spatial electron donor availability.

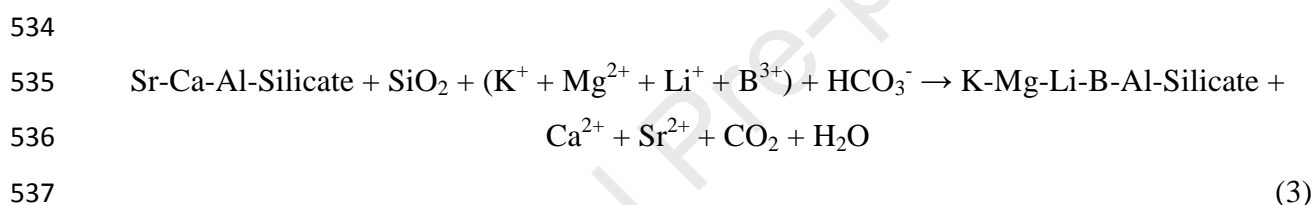
491 POC degradation and methane oxidation could potentially fuel iron reduction at greater  
492 depths (Beal et al., 2009; Egger et al., 2017; Egger et al., 2016), and prevent the development  
493 of well-constrained reaction zones and distinct iron peaks. However, in most cases high  $\text{Fe}^{2+}$   
494 concentrations are constrained to particular intervals with distinct maxima, thus Fe(III)  
495 reduction appears to be controlled by diffusive transport of reactive species to some extent.  
496 Iron reduction could also be driven by DOC degradation. To become available at greater  
497 depths, organic compounds must escape from the sulfate reduction zone. DOC supply to  
498 greater depths could become possible from an excess availability of DOC compared to  
499 sulfate, availability of methane as substrate for sulfate reduction, kinetic limitations of  
500 syntrophic substrate transfer, inhibition of sulfate reduction by high sulfide concentrations, or  
501 the release of non-competing intermediates, which are not available for microbial sulfate  
502 reduction. In principal, the absence of sulfate-reducing microorganisms in lacustrine  
503 sediments could explain DOC transport to greater depth, away from the sulfate reduction  
504 zone. However, so far there is no evidence for this assumption (Leloup et al., 2007). Clearly,  
505 the overall balance (Eq.1) provides very limited mechanistic insight, since sulfate-reducing  
506 microorganisms only metabolize small organic molecules (e.g. volatile fatty acids: VFA) or  
507  $\text{H}_2$ , which are products of hydrolytic and fermentative microbial reactions. Thus, organic  
508 matter degradation and the concomitant release of DOC close to the sediment-water interface,  
509 especially during the high productivity period, could potentially supply substrates for  
510 microbial metabolism at greater depths. Whereas seawater intrusion certainly initiated a  
511 marked shift of the terminal electron-accepting step to microbial sulfate reduction, it is less  
512 clear if and to what extent earlier steps of organic matter degradation have changed, that  
513 means, hydrolysis and fermentation.

514

#### 515 *Diagenetic reactions in response to seawater intrusion*

516 Complementary to interval definition from pore water profiles, diagenetic reactions are  
517 assigned to 3 specific intervals: (1) AOM and microbial sulfate reduction is located in the  
518 interval 0 to 6 mbsf with sulfate depletion to near zero values at the SMTZ, whereas POC is  
519 distributed over the upper 15 mbsf. This upper zone is further characterized by silica  
520 dissolution leading to  $\text{SiO}_4^{4-}$  peaks close to the sediment-water interface. (2) Ion exchange

521 processes with lacustrine clay minerals likely control concentrations of major cations in the  
 522 sediment column above 22-24 mbsf, which results in the net uptake of  $K^+$ ,  $Mg^{2+}$  and  $Na^+$ , and  
 523 the net release of  $Ca^{2+}$  and  $Sr^{2+}$  above 11-13 mbsf. (3) In addition to ion exchange reactions,  
 524 the interval 8-15 mbsf shows clear evidence for reverse weathering reactions and dissolution  
 525 of silicate and/ or carbonate phases, with a net release of  $Mg^{2+}$  in a 1:1 ratio with  $Ca^{2+}$  in the  
 526 interval 11-13 mbsf. Further,  $Fe^{2+}$  and  $Mn^{2+}$  are released between 8-15 mbsf (Fig. 2), which  
 527 indicates that microbial iron and manganese reduction are linked to these mineral reactions.  
 528 Since no alkalinity increase is observed below the SMTZ, TA release from mineral  
 529 weathering or dissolution needs to be balanced by TA consumption. Reverse silicate  
 530 weathering (Eq.3) could consume TA, alkaline and alkaline earth metals, and release  $Ca^{2+}$   
 531 (Aloisi et al., 2004a; Kim et al., 2016; Spivack et al., 1987; Vigier et al., 2008).  
 532 Aluminosilicates such as plagioclase and K-feldspar, which are sufficiently abundant in the  
 533 sediment, are good candidates for marine reverse weathering reactions such as:

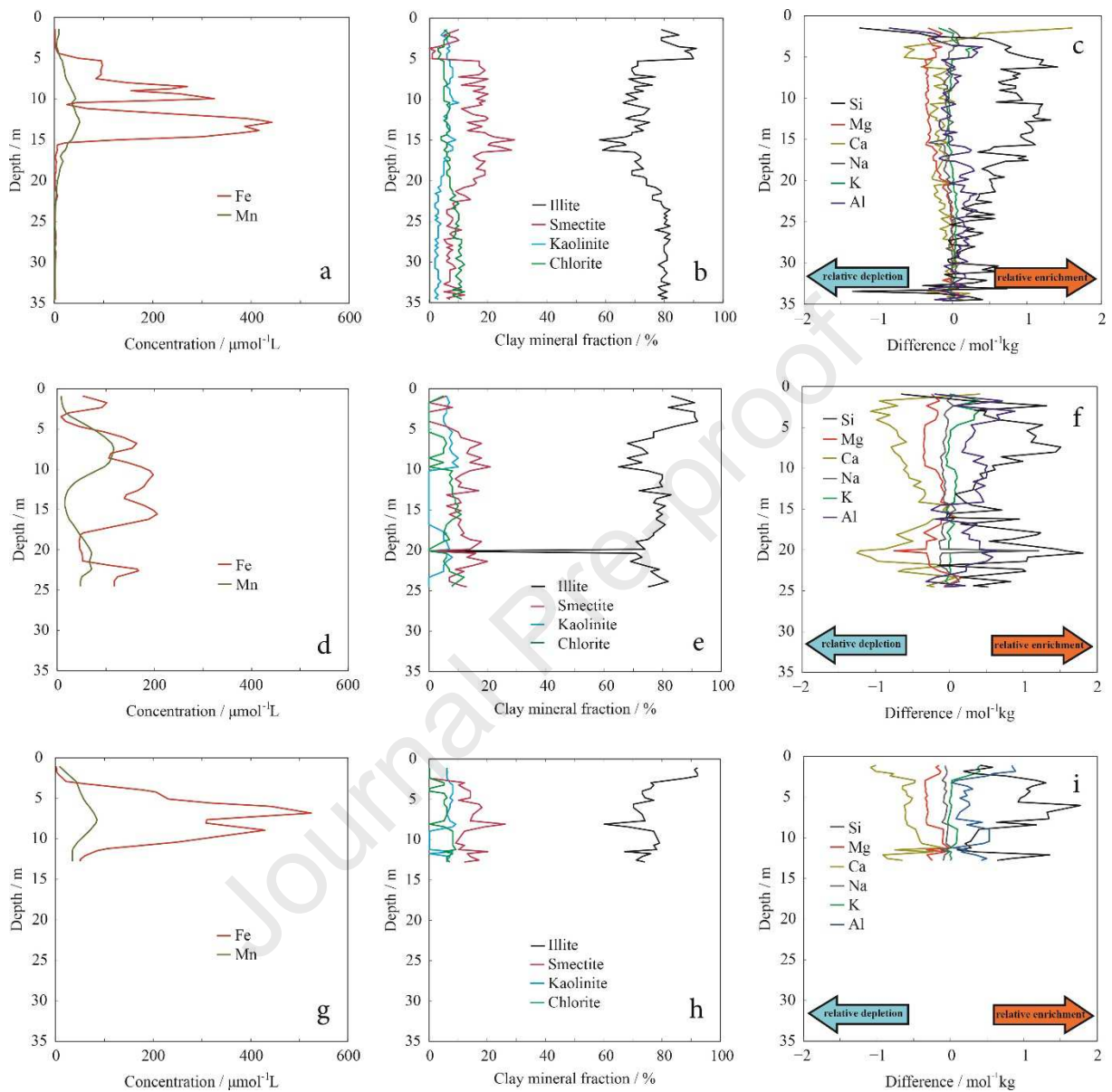


538 From comparing element budgets over depth from cores GAS-CS01, CS03 and CS07  
 539 (Fig. 8c, f and i, respectively), it is suggested that the progress of diagenetic processes since  
 540 the Holocene seawater intrusion is not visible in the sediment element or mineral  
 541 composition, and the chemical signals could not overprint lithological variability. Budgets  
 542 from all cores are evaluated as relative changes compared to element contents in the lower  
 543 parts of GAS-CS01, and unlike pore water profiles, normalized sediment element profiles can  
 544 be linked to stratigraphical features (see supplementary materials for the core logs).

545 The considerable variability in sediment stratigraphy and mineral composition at  
 546 different locations does not have a clear effect on reactive transport and pore water profiles of  
 547 major cations. This could be related to the large pool of reactive minerals or the dominance of  
 548 kinetic controls of slow geochemical reactions. However, the similarity of pore water profiles  
 549 could also be linked to microbial metabolism, which would be regulated by substrate  
 550 availability rather than sediment mineralogy, as discussed above referring to microbial iron  
 551 reduction. Interestingly, the depletion of seawater cations at 22 - 24 mbsf coincides with  
 552 changes in clay mineral composition (Fig. 4, GAS-CS01). While these changes appear to be  
 553 sufficiently explained by variability of sediment sources and input rates during the Late  
 554 Pleistocene and Holocene, as discussed above, we cannot exclude that ion exchange reactions

555 or other diagenetic processes triggered after seawater intrusion contribute to these  
 556 conspicuous shifts.

557



558

559 Fig. 8: Dissolved Fe and Mn profiles (a: GAS-CS01, d: GAS-CS03, g: GAS-CS07), clay mineral composition  
 560 (b: GAS-CS01, e: GAS-CS03, h: GAS-CS07) and sediment composition changes relative to steady state  
 561 compositions below seawater penetration depth at 31-33 mbsf based on  $\text{Cl}^-$  profiles in GAS-CS01 (c: GAS-  
 562 CS01, f: GAS-CS03, i: GAS-CS07).

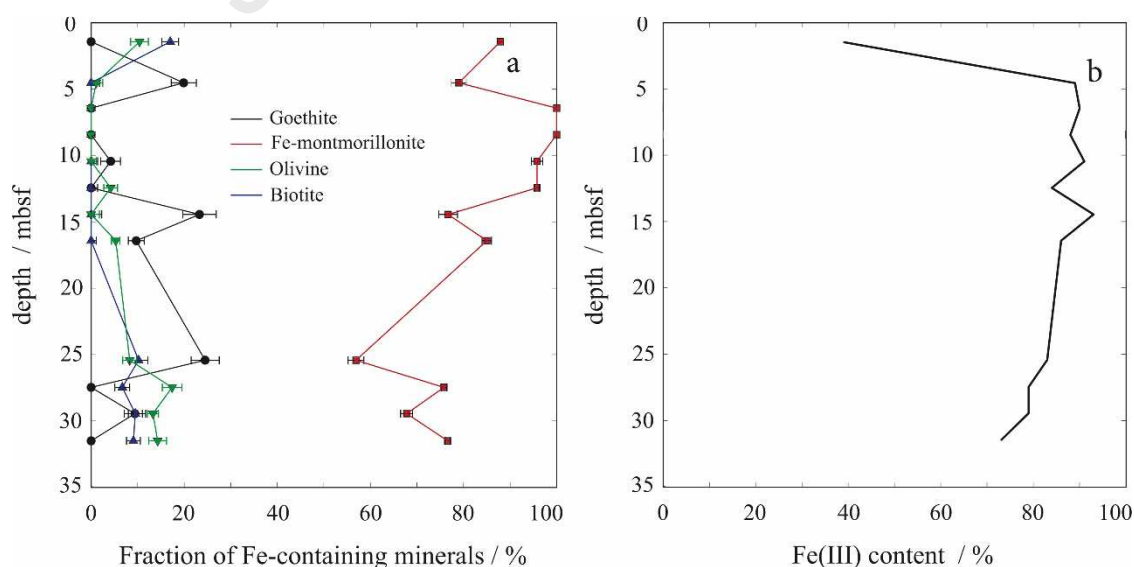
563

564 We hypothesize that the release of  $\text{Fe}^{2+}$  and  $\text{Mn}^{2+}$  through microbial iron and  
 565 manganese reduction was stimulated by the iron and organic substrate availability in response  
 566 to seawater intrusion. Preliminary X-ray absorption data analyses suggest that iron is strongly  
 567 associated with phyllosilicates in interval 2, above 22-24 mbsf (Fig.9a). The actual Fe(III)

568 source, however, is not fully resolved. The analysis of Fe(III):Fe(II) ratios shows a trend of  
 569 increasing Fe(III) content towards shallower sediments depths (Fig.9b), which is  
 570 counterintuitive to expected increased contents of Fe(II) in the iron reduction zone. However,  
 571 smectite-bound Fe(II) is readily oxidized under atmospheric conditions (Rozenson and Heller-  
 572 Kallai, 1978), which would explain the Fe(III):Fe(II) ratios. Sampling and chemical  
 573 procedures in this study were not focused on iron analysis, thus redox effects and long-time  
 574 storage artefacts could influence iron concentration measurements and mineral speciation  
 575 analysis. Iron speciation analysis further suggests, that at greater depths higher amounts of  
 576 iron are associated with other minerals (among our reference minerals, goethite, biotite and  
 577 olivine gave the best results for fitting the deviations from the pure montmorillonite  
 578 spectrum), and Fe(II) contents were better preserved during storage and analysis.

579 Since iron at relevant depths is associated with clay minerals rather than with oxy-  
 580 hydroxide phases, it appears that its reduction could have contributed to clay mineral  
 581 alteration in a direct or indirect way (Kim et al., 2019; Kostka et al., 2002; Liu et al., 2016;  
 582 Liu et al., 2017; Pentráková et al., 2013; Vorhies and Gaines, 2009). Thus, clay mineral  
 583 alteration in the study area could have been influenced by reduction of structurally  
 584 coordinated Fe(III), which would change charge balances and could trigger changes of the  
 585 mineral structure or ion exchange capacities (Meunier and El Albani, 2007). Alternatively, if  
 586 Fe(III) was supplied from an iron oxy-hydroxide phase (e.g. goethite), clay mineral alteration  
 587 could become driven by equilibration of solid solutions with dissolved Fe<sup>2+</sup> or dissolution-  
 588 induced formation of Fe(II)- rich secondary clay minerals.

589



590

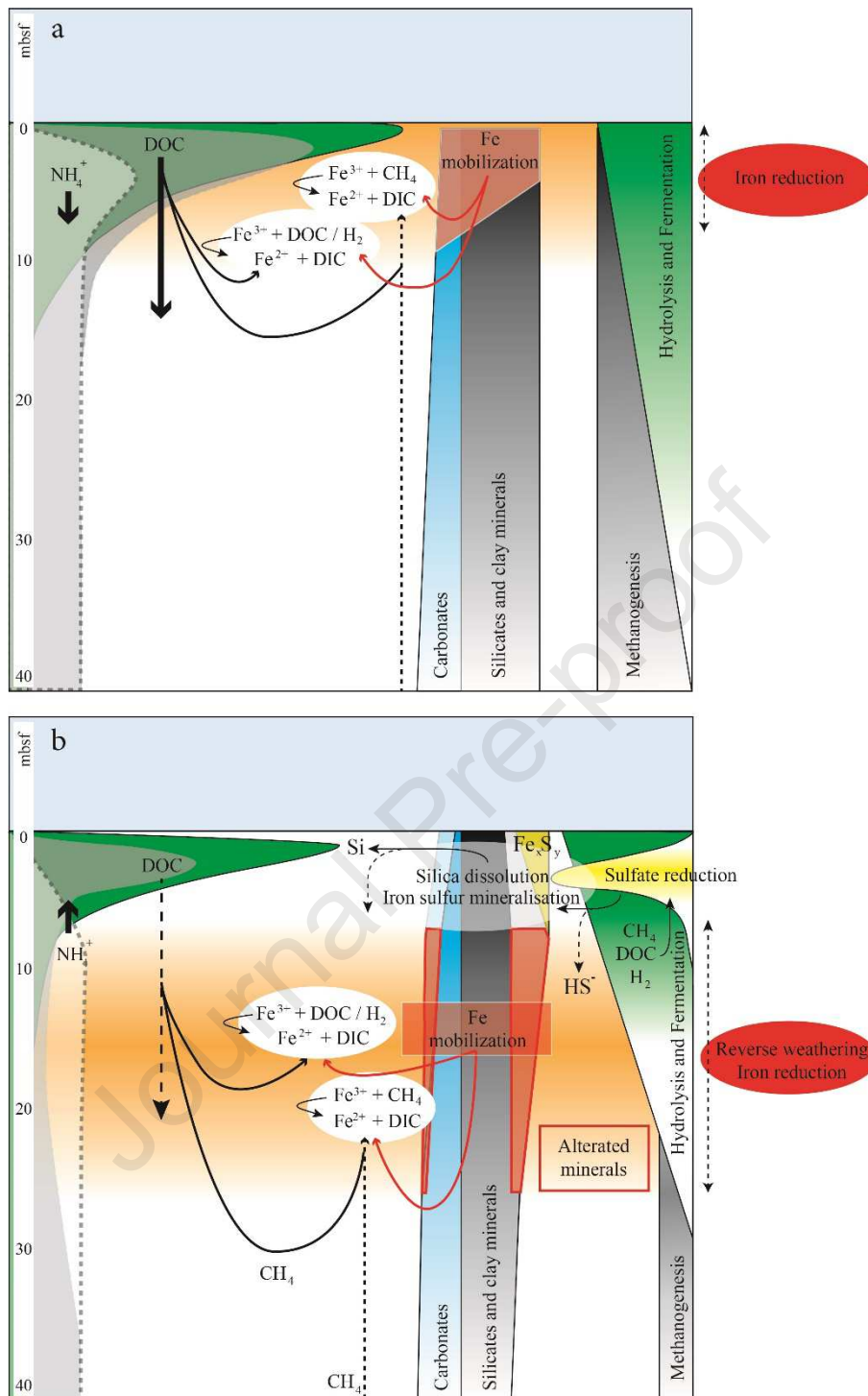
591 Fig. 9: (a) Solid phase iron speciation and (b) Fe(III) content for core GAS-CS01. Fe(III) content determination  
 592 by XANES pre-edge fitting is prone to errors and we had not enough suitable reference samples available for a

593 proper calibration of the results. Therefore, absolute values in this graph are uncertain, but relative trends in  
594 Fe(III) content are reliable.

595

596 Summarizing our discussion in a conceptual model (Fig.10), we propose that chemical  
597 shifts resulting from seawater intrusion and salt diffusion drive reverse weathering reactions  
598 and contribute to the chemical alteration of phyllosilicates. Since iron appears to be largely  
599 associated with clay minerals, the alteration of clay minerals could influence iron  
600 bioavailability, thus opening up a refractory iron pool. In particular, our conceptual model  
601 considers that a redox zonation shift in response to seawater intrusion controls the electron  
602 donor supply for microbial iron reduction, acting as the actual driver for iron reduction at  
603 depth.

604



605

606

607

608

609

610

611

612

Fig. 10: Conceptual model scheme for coupling of biogeochemical processes and element cycling before (a) and after (b) seawater inflow. Prior to seawater intrusion, methanogenesis and microbial Fe reduction were key processes in Black Sea “lake” sediments. In response to seawater intrusion, ion exchange, dissolution and reverse weathering reactions change the composition of minerals in the lacustrine sediment. In addition to that, the development of a shallow sulfate reduction zone shifts microbial iron reduction to greater depths. We hypothesize that both organoclastic and methanotrophic sulfate reduction contribute to the overall sulfate turnover, and that, however, the organic carbon turnover has not become fully adapted to sulfate reduction under

613 transient state conditions. Thus, dissolved organic compounds (i.e. DOC) escape from the sulfate reduction zone  
614 and fuel microbial iron reduction at depth.

615

## 616 **Conclusion**

617 Pore water data show the progress of reactive-transport processes in lacustrine sediments at  
618 the Black Sea western slope after seawater intrusion into the basin 9 ka BP. Intense sulfate  
619 reduction and cation exchange at shallow depths provide clear evidence of ongoing dynamic  
620 alteration of the lacustrine sediments. The seawater intrusion drives the release of  $\text{Ca}^{2+}$  and  
621  $\text{Sr}^{2+}$ , and the uptake of  $\text{K}^+$ ,  $\text{Mg}^{2+}$  and  $\text{Na}^+$  in the sediment through reverse weathering and ion  
622 exchange, and affects clay mineral pools and iron bioavailability below the SMTZ. Post-  
623 depositional disturbances are not clearly visible, and strong sediment and pore water evidence  
624 for mass movement events and slope destabilization is lacking. Similarly, the intense gas  
625 seepage, which guided the choice of coring locations, was not significantly reflected in pore  
626 water profiles, except for a shoaling of the SMTZ. However, the large variability of sediment  
627 composition and mineralogy, which results from highly dynamic changes in solids transport  
628 and deposition rates during the last glacial period and Holocene, strongly complicates the  
629 geochemical interpretations.

630

## 631 **Acknowledgements**

632 We thank the captain and his crew on-board the *RV Pourquoi pas?* crew for their technical  
633 support and advices. Financial support for the cruise was provided by Ifremer and the  
634 European project Midas (grant agreement 603418). This work is also a contribution to the  
635 BLAME project sponsored by the French National Research Agency (ANR-18-CE01-0007)  
636 and the SUGAR project funded by the German Federal Ministry of Economic Affairs and  
637 Energy (grant no. 03SX320A) and the German Federal Ministry of Education and Research  
638 (grant nos. 03G0819A and 03G0856A). We acknowledge DESY (Hamburg, Germany), a  
639 member of the Helmholtz Association HGF, for the provision of experimental facilities. Parts  
640 of this research were carried out at beamline P64 and we would like to thank Wolfgang A.  
641 Caliebe (DESY) for assistance in operating the beamline and Anna-Kathrin Retschko  
642 (GEOMAR) for sample preparation. We thank Andrea Bodenbinder, Bettina Domeyer, Anke  
643 Bleyer and Regina Surberg for the excellent support with shore-based analyses, as well as Dr.  
644 Guillaume Soulet for constructive discussion. We also thank two anonymous reviewers for  
645 their valuable comments, which significantly improved the content of the paper.

646

647 **Reference**

- 648
- 649 Aloisi, G., Drews, M., Wallmann, K., Bohrmann, G., 2004a. Fluid expulsion from the Dvurechenskii  
650 mud volcano (Black Sea): Part I. Fluid sources and relevance to Li, B, Sr, I and dissolved inorganic  
651 nitrogen cycles. *Earth and Planetary Science Letters* 225, 347-363.
- 652 Aloisi, G., Wallmann, K., Drews, M., 2004b. Evidence for the submarine weathering of silicate  
653 minerals in Black Sea sediments: Possible implications for the marine Li and B cycles. *Geochemistry  
654 Geophysics Geosystems* 5.
- 655 Ballas, G., Garziglia, S., Sultan, N., Pelleter, E., Toucanne, S., Marsset, T., Riboulot, V., Ker, S., 2018.  
656 Influence of early diagenesis on geotechnical properties of clay sediments (Romania, Black Sea).  
657 *Engineering Geology* 240, 175-188.
- 658 Bar-Or, I., Elvert, M., Eckert, W., Kushmaro, A., Vigderovich, H., Zhu, Q., Ben-Dov, E., Sivan, O., 2017.  
659 Iron-coupled anaerobic oxidation of methane performed by a mixed bacterial-archaeal community  
660 based on poorly reactive minerals. *Environmental science & technology* 51, 12293-12301.
- 661 Beal, E.J., House, C.H., Orphan, V.J., 2009. Manganese-and iron-dependent marine methane  
662 oxidation. *Science* 325, 184-187.
- 663 Bernard, B.B., Brooks, J.M., Sackett, W.M., 1978. Light-hydrocarbons in recent texas continental-shelf  
664 and slope sediments. *Journal of Geophysical Research-Oceans and Atmospheres* 83, 4053-4061.
- 665 Bialas, J., Klauke, I., Haeckel, M., 2014. FS MARIA S. MERIAN Fahrtbericht / Cruise Report MSM34/1  
666 & 2 - SUGAR Site ; Varna – Varna, 06.12.13 – 16.01.14. GEOMAR Report N. Ser. 015. GEOMAR  
667 Helmholtz-Zentrum für Ozeanforschung, Kiel, Germany, Open Access, DOI  
668 10.3289/GEOMAR\_REP\_NS\_15\_2014, 111 pp.
- 669 Blinova, V.N., Ivanov, M.K., Bohrmann, G., 2003. Hydrocarbon gases in deposits from mud volcanoes  
670 in the Sorokin Trough, north-eastern Black Sea. *Geo-Marine Letters* 23, 250-257.
- 671 Bohrmann, G., Ivanov, M., Foucher, J.P., Spiess, V., Bialas, J., Greinert, J., Weinrebe, W., Abegg, F.,  
672 Aloisi, G., Artemov, Y., Blinova, V., Drews, M., Heidersdorf, F., Krabbenhoft, A., Klauke, I., Krastel, S.,  
673 Leder, T., Polikarpov, I., Saburova, M., Schmale, O., Seifert, R., Volkonskaya, A., Zillmer, M., 2003.  
674 Mud volcanoes and gas hydrates in the Black Sea: new data from Dvurechenskii and Odessa mud  
675 volcanoes. *Geo-Marine Letters* 23, 239-249.
- 676 Borowski, W.S., Paull, C.K., Ussler, W., 1999. Global and local variations of interstitial sulfate  
677 gradients in deep-water, continental margin sediments: Sensitivity to underlying methane and gas  
678 hydrates. *Marine Geology* 159, 131-154.
- 679 Caliebe, W.A., Murzin, V., Kalinko, A., Görlitz, M., 2019. High-flux XAFS-beamline P64 at PETRA III, AIP  
680 Conference Proceedings. AIP Publishing, p. 060031.
- 681 Calvin, S., 2013. XAFS for Everyone. CRC press.
- 682 Canfield, D.E., Raiswell, R., Bottrell, S., 1992. The reactivity of sedimentary iron minerals toward  
683 sulfide. *American Journal of Science* 292, 659-683.
- 684 Constantinescu, A.M., Toucanne, S., Dennielou, B., Jorry, S.J., Mulder, T., Lericolais, G., 2015.  
685 Evolution of the Danube Deep-Sea Fan since the Last Glacial Maximum: new insights into Black Sea  
686 water-level fluctuations. *Marine Geology* 367, 50-68.
- 687 Egger, M., Hagens, M., Sapart, C.J., Dijkstra, N., van Helmond, N., Mogollon, J.M., Risgaard-Petersen,  
688 N., van der Veen, C., Kasten, S., Riedinger, N., Bottcher, M.E., Rockmann, T., Jorgensen, B.B., Slomp,  
689 C.P., 2017. Iron oxide reduction in methane-rich deep Baltic Sea sediments. *Geochimica Et  
690 Cosmochimica Acta* 207, 256-276.
- 691 Egger, M., Kraal, P., Jilbert, T., Sulu-Gambari, F., Sapart, C.J., Rockmann, T., Slomp, C.P., 2016.  
692 Anaerobic oxidation of methane alters sediment records of sulfur, iron and phosphorus in the Black  
693 Sea. *Biogeosciences* 13, 5333-5355.
- 694 Grasshoff, K., Kremling, K., Ehrhardt, M., 1999. *Methods of seawater analysis*, Wiley VCH. Weinheim,  
695 Germany.
- 696 Gregory, D., Mukherjee, I., Olson, S.L., Large, R.R., Danyushevsky, L.V., Stepanov, A.S., Avila, J.N., Cliff,  
697 J., Ireland, T.R., Raiswell, R., Olin, P.H., Maslennikov, V.V., Lyons, T.W., 2019. The formation

- 698 mechanisms of sedimentary pyrite nodules determined by trace element and sulfur isotope  
699 microanalysis. *Geochimica et Cosmochimica Acta* 259, 53-68.
- 700 Greinert, J., Artemov, Y., Egorov, V., De Batist, M., McGinnis, D., 2006. 1300-m-high rising bubbles  
701 from mud volcanoes at 2080m in the Black Sea: Hydroacoustic characteristics and temporal  
702 variability. *Earth and Planetary Science Letters* 244, 1-15.
- 703 Greinert, J., McGinnis, D.F., Naudts, L., Linke, P., De Batist, M., 2010. Atmospheric methane flux from  
704 bubbling seeps: Spatially extrapolated quantification from a Black Sea shelf area. *Journal of*  
705 *Geophysical Research-Oceans* 115.
- 706 Haeckel, M., 2006. A transport-reaction model of the hydrological systems of the Costa Rica  
707 subduction zone, *Proceedings of the Ocean Drilling Program, Scientific Results, Leg*, pp. 1-26.
- 708 Haeckel, M., Bialas, J., Klaucke, I., Wallmann, K., Bohrmann, G., Schwalenberg, K., 2015. Gas hydrate  
709 occurrences in the Black Sea—new observations from the German SUGAR project. *Fire in the Ice:*  
710 *Methane Hydrate Newsletter* 15, 6-9.
- 711 Haffert, L., Haeckel, M., Liebetrau, V., Berndt, C., Hensen, C., Nuzzo, M., Reitz, A., Scholz, F.,  
712 Schonfeld, J., Perez-Garcia, C., Weise, S.M., 2013. Fluid evolution and authigenic mineral paragenesis  
713 related to salt diapirism - The Mercator mud volcano in the Gulf of Cadiz. *Geochimica Et*  
714 *Cosmochimica Acta* 106, 261-286.
- 715 Heeschen, K.U., Haeckel, M., Klaucke, I., Ivanov, M.K., Bohrmann, G., 2011. Quantifying in-situ gas  
716 hydrates at active seep sites in the eastern Black Sea using pressure coring technique. *Biogeosciences*  
717 8, 3555-3565.
- 718 Henkel, S., Mogollon, J.M., Noethen, K., Franke, C., Bogus, K., Robin, E., Bahr, A., Blumenberg, M.,  
719 Pape, T., Seifert, R., Maerz, C., de Lange, G.J., Kasten, S., 2012. Diagenetic barium cycling in Black Sea  
720 sediments - A case study for anoxic marine environments. *Geochimica et Cosmochimica Acta* 88, 88-  
721 105.
- 722 Hillman, J.I.T., Klaucke, I., Bialas, J., Feldman, H., Drexler, T., Awwiller, D., Atgin, O., Cifci, G., Badhani,  
723 S., 2018a. Gas migration pathways and slope failures in the Danube Fan, Black Sea. *Marine and*  
724 *Petroleum Geology* 92, 1069-1084.
- 725 Hillman, J.I.T., Klaucke, I., Bialas, J., Feldman, H., Drexler, T., Awwiller, D., Atgin, O., Çifçi, G., Badhani,  
726 S., 2018b. Gas migration pathways and slope failures in the Danube Fan, Black Sea. *Marine and*  
727 *Petroleum Geology* 92, 1069-1084.
- 728 Holmkvist, L., Kamyshny, A., Jr., Vogt, C., Vamvakopoulos, K., Ferdelman, T.G., Jorgensen, B.B., 2011.  
729 Sulfate reduction below the sulfate-methane transition in Black Sea sediments. *Deep-Sea Research*  
730 *Part I-Oceanographic Research Papers* 58, 493-504.
- 731 Holtzappel, T., 1985. Les minéraux argileux, préparation, analyse diffractométrique et détermination.  
732 *Société Géologique du nord* 12, 1-36.
- 733 Huvaj, Y.N., Huff, W.D., 2016. Clay mineralogy and geochemistry of three offshore wells in the  
734 southwestern Black Sea, northern Turkey: the effect of burial diagenesis on the conversion of  
735 smectite to illite. *Turkish Journal of Earth Sciences* 25, 592-610.
- 736 Jorgensen, B.B., Böttcher, M.E., Lüschen, H., Neretin, L.N., Volkov, I.I., 2004. Anaerobic methane  
737 oxidation and a deep H<sub>2</sub>S sink generate isotopically heavy sulfides in Black Sea sediments.  
738 *Geochimica et Cosmochimica Acta* 68, 2095-2118.
- 739 Jorgensen, B.B., Weber, A., Zopfi, J., 2001. Sulfate reduction and anaerobic methane oxidation in  
740 Black Sea sediments. *Deep-Sea Research Part I-Oceanographic Research Papers* 48, 2097-2120.
- 741 Ker, S., Thomas, Y., Riboulot, V., Sultan, N., Bernard, C., Scalabrin, C., Ion, G., Marsset, B., 2019.  
742 Anomalously Deep BSR Related to a Transient State of the Gas Hydrate System in the Western Black  
743 Sea. *Geochemistry Geophysics Geosystems* 20, 442-459.
- 744 Kessler, J.D., Reeburgh, W.S., Southon, J., Seifert, R., Michaelis, W., Tyler, S.C., 2006a. Basin-wide  
745 estimates of the input of methane from seeps and clathrates to the Black Sea. *Earth and Planetary*  
746 *Science Letters* 243, 366-375.
- 747 Kessler, J.D., Reeburgh, W.S., Tyler, S.C., 2006b. Controls on methane concentration and stable  
748 isotope ( $\delta$  H-2-CH<sub>4</sub> and  $\delta$  C-13-CH<sub>4</sub>) distributions in the water columns of the Black Sea and  
749 Cariaco Basin. *Global biogeochemical cycles* 20.

- 750 Kim, J., Dong, H., Yang, K., Park, H., Elliott, W.C., Spivack, A., Koo, T., Kim, G., Morono, Y., Henkel, S.,  
751 Inagaki, F., Zeng, Q., Hoshino, T., Heuer, V.B., 2019. Naturally occurring, microbially induced  
752 smectite-to-illite reaction. *Geology* 47, 535-539.
- 753 Kim, J.H., Torres, M.E., Haley, B.A., Ryu, J.S., Park, M.H., Hong, W.L., Choi, J., 2016. Marine silicate  
754 weathering in the anoxic sediment of the Ulleung Basin: Evidence and consequences. *Geochemistry  
755 Geophysics Geosystems* 17, 3437-3453.
- 756 Knab, N.J., Cragg, B.A., Hornibrook, E.R.C., Holmkvist, L., Pancost, R.D., Borowski, C., Parkes, R.J.,  
757 Jørgensen, B.B., 2009. Regulation of anaerobic methane oxidation in sediments of the black sea.  
758 *Biogeosciences* 6, 1505-1518.
- 759 Kosarev, A.N., 2007. *The Black Sea Environment*. Springer.
- 760 Kostka, J.E., Dalton, D.D., Skelton, H., Dollhopf, S., Stucki, J.W., 2002. Growth of iron (III)-reducing  
761 bacteria on clay minerals as the sole electron acceptor and comparison of growth yields on a variety  
762 of oxidized iron forms. *Appl. Environ. Microbiol.* 68, 6256-6262.
- 763 Kraal, P., Yucel, M., Slomp, C.P., 2019. Turbidite deposition and diagenesis in the southwestern Black  
764 Sea: Implications for biogeochemical cycling in an anoxic basin. *Marine Chemistry* 209, 48-61.
- 765 Leloup, J., Loy, A., Knab, N.J., Borowski, C., Wagner, M., Jørgensen, B.B., 2007. Diversity and  
766 abundance of sulfate-reducing microorganisms in the sulfate and methane zones of a marine  
767 sediment, Black Sea. *Environmental microbiology* 9, 131-142.
- 768 Lericolais, G., Bourget, J., Popescu, I., Jermannaud, P., Mulder, T., Jorry, S., Panin, N., 2013. Late  
769 Quaternary deep-sea sedimentation in the western Black Sea: New insights from recent coring and  
770 seismic data in the deep basin. *Global and Planetary Change* 103, 232-247.
- 771 Liu, D., Wang, F., Dong, H., Wang, H., Zhao, L., Huang, L., Wu, L., 2016. Biological reduction of  
772 structural Fe(III) in smectites by a marine bacterium at 0.1 and 20 MPa. *Chemical Geology* 438, 1-10.
- 773 Liu, D., Xu, Y., Papineau, D., Yu, N., Fan, Q., Qiu, X., Wang, H., 2019. Experimental evidence for abiotic  
774 formation of low-temperature proto-dolomite facilitated by clay minerals. *Geochimica et  
775 Cosmochimica Acta* 247, 83-95.
- 776 Liu, G., Qiu, S., Liu, B., Pu, Y., Gao, Z., Wang, J., Jin, R., Zhou, J., 2017. Microbial reduction of Fe(III)-  
777 bearing clay minerals in the presence of humic acids. *Scientific Reports* 7.
- 778 Lyons, T.W., 1997. Sulfur isotopic trends and pathways of iron sulfide formation in upper Holocene  
779 sediments of the anoxic Black Sea. *Geochimica Et Cosmochimica Acta* 61, 3367-3382.
- 780 Major, C.O., Goldstein, S.L., Ryan, W.B.F., Lericolais, G., Piotrowski, A.M., Hajdas, I., 2006. The co-  
781 evolution of Black Sea level and composition through the last deglaciation and its paleoclimatic  
782 significance. *Quaternary Science Reviews* 25, 2031-2047.
- 783 Martinez-Lamas, R., Toucanne, S., Debret, M., Riboulot, V., Deloffre, J., Boissier, A., Cheron, S., Pitel,  
784 M., Bayon, G., Giosan, L., 2020. Linking Danube River activity to Alpine Ice-Sheet fluctuations during  
785 the last glacial (ca. 33–17 ka BP): Insights into the continental signature of Heinrich Stadials.  
786 *Quaternary Science Reviews* 229, 106136.
- 787 Meister, P., Brunner, B., Picard, A., Böttcher, M.E., Jørgensen, B.B., 2019. Sulphur and carbon  
788 isotopes as tracers of past sub-seafloor microbial activity. *Scientific reports* 9, 1-9.
- 789 Meister, P., Liu, B., Ferdelman, T.G., Jørgensen, B.B., Khalili, A., 2013. Control of sulphate and  
790 methane distributions in marine sediments by organic matter reactivity. *Geochimica et  
791 Cosmochimica Acta* 104, 183-193.
- 792 Meunier, A., El Albani, A., 2007. The glauconite-Fe-illite-Fe-smectite problem: A critical review. *Terra  
793 Nova* 19, 95-104.
- 794 Naudts, L., Greinert, J., Artemov, Y., Staelens, P., Poort, J., Van Rensbergen, P., De Batist, M., 2006.  
795 Geological and morphological setting of 2778 methane seeps in the Dnepr paleo-delta, northwestern  
796 Black Sea. *Marine Geology* 227, 177-199.
- 797 Neretin, L.N., Volkov, I.I., Böttcher, M.E., Grinenko, V.A., 2001. A sulfur budget for the Black Sea  
798 anoxic zone. *Deep Sea Research Part I: Oceanographic Research Papers* 48, 2569-2593.
- 799 Niewohner, C., Hensen, C., Kasten, S., Zabel, M., Schulz, H.D., 1998. Deep sulfate reduction  
800 completely mediated by anaerobic methane oxidation in sediments of the upwelling area off  
801 Namibia. *Geochimica et Cosmochimica Acta* 62, 455-464.

- 802 Noethen, K., Kasten, S., 2011. Reconstructing changes in seep activity by means of pore water and  
803 solid phase Sr/Ca and Mg/Ca ratios in pockmark sediments of the Northern Congo Fan. *Marine*  
804 *Geology* 287, 1-13.
- 805 Oni, O., Miyatake, T., Kasten, S., Richter-Heitmann, T., Fischer, D., Wagenknecht, L., Kulkarni, A.,  
806 Blumers, M., Shylin, S.I., Ksenofontov, V., Costa, B.F.O., Klingelhofer, G., Friedrich, M.W., 2015.  
807 Distinct microbial populations are tightly linked to the profile of dissolved iron in the methanic  
808 sediments of the Helgoland mud area, North Sea. *Frontiers in Microbiology* 6.
- 809 Özsoy, E., Ünlüata, Ü., 1997. Oceanography of the Black Sea: a review of some recent results. *Earth-*  
810 *Science Reviews* 42, 231-272.
- 811 Pape, T., Blumenberg, M., Seifert, R., Bohrmann, G., Michaelis, W., 2008. Marine Methane  
812 Biogeochemistry of the Black Sea: A Review, in: Dilek, Y.F.H.M.K. (Ed.), *Links between Geological*  
813 *Processes, Microbial Activities & Evolution of Life: Microbes and Geology*, pp. 281-311.
- 814 Pentráková, L., Su, K., Pentrák, M., Stucki, J., 2013. A review of microbial redox interactions with  
815 structural Fe in clay minerals. *Clay Minerals* 48, 543-560.
- 816 Piper, D.Z., Calvert, S., 2011. Holocene and late glacial palaeoceanography and palaeolimnology of  
817 the Black Sea: changing sediment provenance and basin hydrography over the past 20,000 years.  
818 *Geochimica et Cosmochimica Acta* 75, 5597-5624.
- 819 Popescu, I., De Batist, M., Lericolais, G., Nouze, H., Poort, J., Panin, N., Versteeg, W., Gillet, H., 2006.  
820 Multiple bottom-simulating reflections in the Black Sea: Potential proxies of past climate conditions.  
821 *Marine Geology* 227, 163-176.
- 822 Popescu, I., Lericolais, G., Panin, N., De Batist, M., Gillet, H., 2007. Seismic expression of gas and gas  
823 hydrates across the western Black Sea. *Geo-Marine Letters* 27, 173-183.
- 824 Popescu, I., Lericolais, G., Panin, N., Normand, A., Dinu, C., Le Drezen, E., 2004. The Danube  
825 submarine canyon (Black Sea): morphology and sedimentary processes. *Marine Geology* 206, 249-  
826 265.
- 827 Ravel, B., Newville, M., 2005. ATHENA, ARTEMIS, HEPHAESTUS: data analysis for X-ray absorption  
828 spectroscopy using IFEFFIT. *Journal of synchrotron radiation* 12, 537-541.
- 829 Reeburgh, W.S., 2007. Oceanic methane biogeochemistry. *Chemical Reviews* 107, 486-513.
- 830 Reeburgh, W.S., Ward, B.B., Whalen, S.C., Sandbeck, K.A., Kilpatrick, K.A., Kerkhof, L.J., 1991. Black-  
831 sea methane geochemistry. *Deep-Sea Research Part a-Oceanographic Research Papers* 38, S1189-  
832 S1210.
- 833 Regnier, P., Dale, A.W., Arndt, S., LaRowe, D., Mogollon, J., Van Cappellen, P., 2011. Quantitative  
834 analysis of anaerobic oxidation of methane (AOM) in marine sediments: A modeling perspective.  
835 *Earth-Science Reviews*.
- 836 Reitz, A., Pape, T., Haeckel, M., Schmidt, M., Berner, U., Scholz, F., Liebetrau, V., Aloisi, G., Weise,  
837 S.M., Wallmann, K., 2011. Sources of fluids and gases expelled at cold seeps offshore Georgia,  
838 eastern Black Sea. *Geochimica et Cosmochimica Acta* 75, 3250-3268.
- 839 Riboulot, V., Cattaneo, A., Scalabrin, C., Gaillot, A., Jouet, G., Ballas, G., Marsset, T., Garziglia, S., Ker,  
840 S., 2017. Control of the geomorphology and gas hydrate extent on widespread gas emissions  
841 offshore Romania. *Bulletin De La Societe Geologique De France* 188.
- 842 Riboulot, V., Ker, S., Sultan, N., Thomas, Y., Marsset, B., Scalabrin, C., Ruffine, L., Boulart, C., Ion, G.,  
843 2018. Freshwater lake to salt-water sea causing widespread hydrate dissociation in the Black Sea.  
844 *Nature Communications* 9.
- 845 Robinson, A., Rudat, J., Banks, C., Wiles, R., 1996. Petroleum geology of the Black Sea. *Marine and*  
846 *Petroleum Geology* 13, 195-223.
- 847 Robinson, A.G., 1997. Regional and Petroleum Geology of the Black Sea and Surrounding Region:  
848 AAPG Memoir 68. AAPG.
- 849 Roemer, M., Sahling, H., Pape, T., Bahr, A., Feseker, T., Wintersteller, P., Bohrmann, G., 2012.  
850 Geological control and magnitude of methane ebullition from a high-flux seep area in the Black Sea-  
851 the Kerch seep area. *Marine Geology* 319, 57-74.
- 852 Rozenson, I., Heller-Kallai, L., 1978. Reduction and oxidation of Fe 3+ in dioctahedral smectites—III.  
853 Oxidation of octahedral iron in montmorillonite. *Clays and Clay Minerals* 26, 88-92.

- 854 Schmale, O., Beaubien, S.E., Rehder, G., Greinert, J., Lombardi, S., 2010a. Gas seepage in the Dnepr  
855 paleo-delta area (NW-Black Sea) and its regional impact on the water column methane cycle. *Journal*  
856 *of Marine Systems* 80, 90-100.
- 857 Schmale, O., Greinert, J., Rehder, G., 2005. Methane emission from high-intensity marine gas seeps in  
858 the Black Sea into the atmosphere. *Geophysical Research Letters* 32.
- 859 Schmale, O., Haeckel, M., McGinnis, D.F., 2011. Response of the Black Sea methane budget to  
860 massive short-term submarine inputs of methane. *Biogeosciences* 8, 911-918.
- 861 Schmale, O., von Deimling, J.S., Gulzow, W., Nausch, G., Waniek, J.J., Rehder, G., 2010b. Distribution  
862 of methane in the water column of the Baltic Sea. *Geophysical Research Letters* 37.
- 863 Scholz, F., Löscher, C.R., Fiskal, A., Sommer, S., Hensen, C., Lomnitz, U., Wuttig, K., Göttlicher, J.,  
864 Kossel, E., Steininger, R., 2016. Nitrate-dependent iron oxidation limits iron transport in anoxic ocean  
865 regions. *Earth and Planetary Science Letters* 454, 272-281.
- 866 Schouten, S., Wakeham, S.G., Damsté, J.S.S., 2001. Evidence for anaerobic methane oxidation by  
867 archaea in euxinic waters of the Black Sea. *Organic Geochemistry* 32, 1277-1281.
- 868 Seeberg-Elverfeldt, J., Schlüter, M., Feseker, T., Kölling, M., 2005. Rhizon sampling of pore waters  
869 near the sediment/water interface of aquatic systems. *Limnology and oceanography: Methods* 3,  
870 361-371.
- 871 Soulet, G., Delaygue, G., Vallet-Coulomb, C., Bottcher, M.E., Sonzogni, C., Lericolais, G., Bard, E.,  
872 2010. Glacial hydrologic conditions in the Black Sea reconstructed using geochemical pore water  
873 profiles. *Earth and Planetary Science Letters* 296, 57-66.
- 874 Soulet, G., Menot, G., Bayon, G., Rostek, F., Ponzevera, E., Toucanne, S., Lericolais, G., Bard, E., 2013.  
875 Abrupt drainage cycles of the Fennoscandian Ice Sheet. *Proc. Natl. Acad. Sci. U. S. A.* 110, 6682-6687.
- 876 Soulet, G., Menot, G., Garreta, V., Rostek, F., Zaragosi, S., Lericolais, G., Bard, E., 2011a. Black Sea  
877 "Lake" reservoir age evolution since the Last Glacial - Hydrologic and climatic implications. *Earth and*  
878 *Planetary Science Letters* 308, 245-258.
- 879 Soulet, G., Menot, G., Lericolais, G., Bard, E., 2011b. A revised calendar age for the last reconnection  
880 of the Black Sea to the global ocean. *Quaternary Science Reviews* 30, 1019-1026.
- 881 Spivack, A.J., Palmer, M.R., Edmond, J.M., 1987. The sedimentary cycle of the boron isotopes.  
882 *Geochimica et Cosmochimica Acta* 51, 1939-1949.
- 883 Stoffers, P., Muller, G., 1972. Clay mineralogy of Black Sea sediments. *Sedimentology* 18, 113-121.
- 884 Underwood, M.B., Pickering, K.T., 1996. Clay-mineral provenance, sediment dispersal patterns, and  
885 mudrock diagenesis in the Nankai accretionary prism, southwest Japan. *Clays and Clay Minerals* 44,  
886 339-356.
- 887 van Bodegom, P.M., Scholten, J.C.M., Stams, A.J.M., 2004. Direct inhibition of methanogenesis by  
888 ferric iron. *Fems Microbiology Ecology* 49, 261-268.
- 889 Vigderovich, H., Liang, L., Herut, B., Wang, F., Wurgaft, E., Rubin-Blum, M., Sivan, O., 2019. Evidence  
890 for microbial iron reduction in the methanic sediments of the oligotrophic southeastern  
891 Mediterranean continental shelf. *Biogeosciences* 16, 3165-3181.
- 892 Vigier, N., Decarreau, A., Millot, R., Carignan, J., Petit, S., France-Lanord, C., 2008. Quantifying Li  
893 isotope fractionation during smectite formation and implications for the Li cycle. *Geochimica Et*  
894 *Cosmochimica Acta* 72, 780-792.
- 895 Vorhies, J.S., Gaines, R.R., 2009. Microbial dissolution of clay minerals as a source of iron and silica in  
896 marine sediments. *Nature Geoscience* 2, 221-225.
- 897 Wallmann, K., Drews, M., Aloisi, G., Bohrmann, G., 2006. Methane discharge into the Black Sea and  
898 the global ocean via fluid flow through submarine mud volcanoes. *Earth and Planetary Science*  
899 *Letters* 248, 545-560.
- 900 Wegwerth, A., Ganopolski, A., Menot, G., Kaiser, J., Dellwig, O., Bard, E., Lamy, F., Arz, H.W., 2015.  
901 Black Sea temperature response to glacial millennial-scale climate variability. *Geophysical Research*  
902 *Letters* 42, 8147-8154.
- 903 Wegwerth, A., Kaiser, J., Dellwig, O., Shumilovskikh, L.S., Nowaczyk, N.R., Arz, H.W., 2016. Northern  
904 hemisphere climate control on the environmental dynamics in the glacial Black Sea "Lake".  
905 *Quaternary Science Reviews* 135, 41-53.

- 906 Wilke, M., Farges, F., Petit, P.-E., Brown Jr, G.E., Martin, F., 2001. Oxidation state and coordination of  
907 Fe in minerals: An Fe K-XANES spectroscopic study. *American Mineralogist* 86, 714-730.
- 908 Xu, C.L., Greinert, J., Haeckel, M., Bialas, J., Dimitrov, L., Zhao, G.T., 2018. The Character and  
909 Formation of Elongated Depressions on the Upper Bulgarian Slope. *Journal of Ocean University of*  
910 *China* 17, 555-562.
- 911 Zander, T., Haeckel, M., Berndt, C., Chi, W.C., Klaucke, I., Bialas, J., Klaeschen, D., Koch, S., Atgm, O.,  
912 2017. On the origin of multiple BSRs in the Danube deep-sea fan, Black Sea. *Earth and Planetary*  
913 *Science Letters* 462, 15-25.
- 914 Zander, T., Haeckel, M., Klaucke, I., Bialas, J., Klaeschen, D., Papenberg, C., Pape, T., Berndt, C.,  
915 Bohrmann, G., 2020. New insights into geology and geochemistry of the Kerch seep area in the Black  
916 Sea. *Marine and Petroleum Geology* 113, 104162.
- 917 Zhang, J., Dong, H., Liu, D., Fischer, T.B., Wang, S., Huang, L., 2012. Microbial reduction of Fe (III) in  
918 illite–smectite minerals by methanogen *Methanosarcina mazei*. *Chemical Geology* 292, 35-44.
- 919

- Geochemical analyses highlight multiple diagenesis processes occurring in the sediment
- Intense methane seepages and organic matter degradation contribute to the sulfate reduction
- Chemical of dissolved and mineral iron species indicate that iron is associated with clay minerals
- In response to seawater intrusion, ion exchange, dissolution and reverse weathering reactions change the composition of clay constituting the sediment

Journal Pre-proof

**Declaration of interests**

The authors declare that they have no known competing financial interests or personal relationships that could have appeared to influence the work reported in this paper.

The authors declare the following financial interests/personal relationships which may be considered as potential competing interests:

Journal Pre-proof